Robust design of damping controller for power system using a combination of snake optimisation algorithm and optimal control theory

Niharika Agrawal, Faheem Ahmed Khan, Mamatha Gowda

Robust design of damping controller for power system using a combination of snake optimisation algorithm and optimal control theory

Niharika Agrawal* and Faheem Ahmed Khan

Department of Electrical and Electronics Engineering,
Ghousia College of Engineering,
Ramanagaram District – 562 159, Karnataka, India
Email: niharika.svits@gmail.com
Email: faheemahmedkhan11@gmail.com
*Corresponding author

Mamatha Gowda

Department of Artificial Intelligence and Data Science,
BGS College of Engineering and Technology,
Mahalakshmi Puram, Bengaluru, 560 086, Karnataka, India
Email: mahesh.mamatha@gmail.com

Abstract: Low-frequency oscillations (LFO) are created in the power system due to various disturbances. The LFO if not controlled, grows and causes the system separation. There is a huge financial loss due to the interruption of the power supply caused by disturbances. With the increasing complexity of the modern power system, there is a need for the design of a more accurate and detailed modelling. An Advanced Heffron Phillips Model (AHPM) is developed with a higher order Synchronous Generator Model 1.1, based on ten K-Constants for stability improvement. This AHPM employs the combination of snake optimisation algorithm (SOA) and linear quadratic regulator (LQR) from optimal control theory. The highest damping ratio (99.98%) is obtained by AHPM in coordination with PSS, and TCSC based on SOA and LQR. For various parameters, the settling time ranges from 1.5 to 2.0 seconds. This AHPM is robust and capable of meeting the challenges of grid integration with renewables.

Keywords: algorithm; damping; efficient; modelling; oscillations; power system; robust; stability; low-frequency oscillations; LFO; snake optimisation algorithm; SOA; linear quadratic regulator; LQR.

Biographical notes: Niharika Agrawal received her BE and ME in Electrical Engineering from the S.G.S.I.T.S. Engineering College, Madhya Pradesh (Indore). She has worked as an Assistant Professor in the Electrical and Electronics Engineering Department in Madhya Pradesh and Bangalore. Currently, she is working towards her PhD at the Ghousia College of Engineering, Ramanagaram, Karnataka from VTU. Her research interest includes power system, renewable energy, microgrids, soft computing, control systems, and power quality.

Faheem Ahmed Khan is a Professor and the Director of Research and Development in the Department of EEE, Ghousia College of Engineering, Ramanagaram in Karnataka state of India. He completed his Bachelor's in Engineering from SJCE Mysore and Master's degree from UVCE, Bengaluru and completed his PhD from JNTU Hyderabad in the field of High Voltage Engineering. He has presented over 50 papers in national and international journals including IEEE – TDEI. His research area includes high voltage engineering, power system engineering and control engineering. He has 25 years of teaching and two years of industrial experience. He has been awarded with 'Award for Research Publications' from Vision Group on Science and Technology (VGST), Karnataka.

Mamatha Gowda received her Bachelor's degree from the Mangalore University, Master's degree from Bangalore and Doctorate degree from the Prairie View A&M University, Texas, USA in the field of Electrical Engineering. She has 17 years of teaching experience and five years of industrial experience. Her areas of research interest are power electronics, motor drives and controls, renewable energy, power systems and control systems. Currently, she is serving as a Professor and the Head in the AI and DS Department at BGS College of Engineering and Technology, Bangalore.

1   Introduction

Power system plays a pivotal role in the technical and economic development of the country. The smooth operation of the power system is hampered due to disturbances like random changes in load demand, imbalance between requirement and generation of power, network outages, tripping of a line, faults, etc. Low-frequency oscillations are created in the system due to various disturbances and are in the range of 0.1 Hz up to a couple of Hz. In 1996, there was an outage of Western Systems Coordinating Council in North America. The oscillations were triggered due to the loss of a 500 kV line which affected nearly 7.5 million customers and it continued for around nine hours with huge economic loss. The LFO restricts the power transfer capacity of the system (Aribowo et al., 2023). The existing power system is forced to work near stability limits to meet the rising power demand which creates LFO. The LFO is observed due to the interconnection of large power systems by relatively weak lines. Industries like information technology, electronics, communication, etc. are becoming more and more sensitive to power hence power engineers are facing the challenge of providing safe, reliable, and continuous power. The LFO hampers the continuous and quality supply of power. Hence, an efficient and robust damping controller is required for meeting these challenges associated with LFO.

The small signal stability (SSS) is essential for the safe and satisfactory operation of the power system. In SSS the magnitude of disturbance is small. The power system is highly complex and nonlinear. For assessing the SSS, the linearised model is developed with Taylor's series method. The stability features of a synchronous machine under a small perturbation are studied with the single machine infinite bus system (SMIBS). The SMIBS is mathematically analysed in the Heffron-Philips (HP) Model and this model is used for assessing the SSS of the system. The LFO are associated with SSS. The synchronous machine's electromagnetic torque changes as a result of a perturbation. This

torque can be divided into two parts: the damping torque $[(T_D)]$ and the synchronising torque (T_S). For the system to operate steadily, these two torques are necessary. The absence of T_S hampers the synchronous operation and absence of T_D results in LFO. The automatic voltage regulator (AVR) with high gain and fast action added to the system improved the (T_S) but did not guarantee for providing the adequate (T_D). Hence an additional/supplementary controller called a power system stabiliser (PSS) is added with AVR to provide the necessary damping torque. The conventional PSS is designed for a fixed operating point hence when the operating conditions change the PSS is found inadequate. The PSS is effective in providing damping to local modes of oscillations (0.8 to 2.0 Hz) (Izdebski et al., 2022) The PSS may affect the voltage profile adversely and may cause leading power factor (Nocoń and Paszek, 2023). There are inter-area modes of oscillation (0.1–0.7 Hz), which affect the security and stability of the system. The series-controlled FACTS device TCSC is added with PSS for damping both modes of oscillation in the system. The TCSC device is a power electronics-based device, is very economical, and produces fast results (Behzadpoor et al., 2022). The proper coordination between PSS and TCSC is essential to prevent destabilising interaction.

Numerous structures, tools, algorithms, and methods have been employed to increase the stability like bacteria foraging (Panda et al., 2013; Parvandeh et al., 2021), improved Harris Hawk (Chaib et al., 2021), tunicate swarm algorithm-neural network (Aribowo et al., 2021), statistical t-test (Thu et al., 2021), quantum algorithm (Kim and Ahn, 2021), delay-dependent dynamic output feedback controller (Sun et al., 2021), machine learning (Samal et al., 2021), time delay approach (Sahu et al., 2022b), modified arithmetic optimisation (Izci, 2022), type-2 fuzzy lead-lag structure (Khampariya et al., 2022), whale optimisation (Sahu et al., 2022a), improved particle swarm (Latif et al., 2022), steepest descent algorithm (He et al., 2022), PSO and differential evolution (Jokarzadeh et al., 2019; Dao et al., 2023). There has been an improvement in stability with these methods and algorithms. But it is a fact that there is always a scope for further improvement. According to the no free lunch (NFL) theorem one algorithm cannot solve all the different types of problems. One algorithm is good in solving problems related to some area but it may not be so excellent in solving problems related to some other area. This NFL theory motivated to take the challenge of solving the LFO problem with a novel meta-heuristic algorithm known as the snake optimisation algorithm (SOA) which has the key features of exploration and exploitation (Hashim and Hussien, 2022).

The linear quadratic regulator (LQR) methodology from optimal control theory (OCT) is implemented in the present work to develop a robust power system. In LQR there is an innovative and quadratic objective function composed of a weight function of two functions. The first part comprises the state vector and the second part comprises the system input. The two weighting matrices Q and R regulate the excursion in state variables and control effort respectively (Shankar et al., 2019). In LQR, there is a combination of state variables and control effort signal. It is essential to meet the time desired time domain characteristics like minimum rise time, settling time, and peak overshoot along with robustness which is possible with LQR. A system is robust when the system remains stable against all disturbances, operating conditions, modelling errors, neglected dynamics, approximation errors, and parametric uncertainties. The LQR assures such a robust system. In conventional methods, though the system may be stable the oscillations of system variables take an unbearably and undesirably long time to

dampen out. In an LQR-based controller, robustness is achieved by considering several operating conditions (Reddy and Ramanathan, 2017).

The traditional HP model for power systems is developed with synchronous generator (SG) model 1.0.In this SG model 1.0 the damper windings in the d and q-axis are neglected. This model, which only considered the field winding ('f') circuit dynamics on the d (direct)-axis, is third-order. This is one-axis flux decay model (Soliman et al., 2011). The system matrix consists of only four state variables. In this model, only the dynamics of the q-axis internal voltage is considered and the dynamics of the d-axis internal voltage are neglected (Aribowo, 2023). All of the crucial system parameters are included in a thorough mathematical modelling so that differential equations can be used to depict the system's behaviour. In this work, a higher order SG model 1.1 is chosen for designing the HP model and this model is called an Advanced Heffron-Phillips Model (AHPM). There are now five state variables in the system A matrix. In this SG model 1.1, there is a field winding ('f') on the d-axis (direct axis) and one damper winding on the quadrature (q-axis). It is a fourth-order and detailed model for stability studies and is known as a two-axis model. In this SG model, the exciter dynamics can be included easily and hence is preferred for damping contribution analysis. Here the dynamics of both the q and d axes' internal voltages are considered in mathematical modelling. This is a better and more advanced model for stability improvement. This work related to mathematical modelling consists of all the essential steps like building a model, analysis of its behaviour, and evaluation of the model.

With the integration of renewables in the grid there are unpredictable and unforeseen conditions. There is a reduction in stored kinetic energy due to wind farms and photo voltaic (PV) (Abdulkader et al., 2023). The PV affects the damping of interarea modes of oscillations in addition to the mode shapes. Different oscillation modes are created because of the erroneous setting of control parameters in PV. The power system has to compromise for stability due to renewables. But now with better and more detailed mathematical modelling and the inclusion of dynamics of d-axis internal voltage, the AHPM is capable of meeting the issues and challenges of grid stability with renewables. The TCSC provides inherent benefits like improving the power transfer capacity of the system, better voltage profile, damping oscillations, meeting transient stability, and SSR mitigation. The simulation work is done with MATLAB R2020a on an Intel(R) Core(TM) i5-7200U CPU @ 2.50GHz, 2.70 GHz processor with 64-bit operating system, x64-based processor, and installed RAM of 8.00 GB.

Primary contributions of this paper are:

- Meeting the challenges related to LFO and improving the stability of the system.

- Development of an AHPM without neglecting the dynamics.

- Tuning the parameters by a novel SOA which has been tested on Congress on Evolutionary Computation (CEC) 2017 benchmark functions.

- Application of twin technologies: the optimisation algorithm and OCT.

- Capability to meet the challenges of grid integration with renewables related to stability and power quality.

- Application of LQR methodology based on an innovative quadratic objective function.

- Capability to control the amplitude of state and control signals with the help of Q and R weighting matrices. With LQR, no compromise is required between the speed of the controller and control effort.

- Modelling the AHPM with SG model 1.1 helps in the early detection of instability in the system and its origin.

- The robust design of the damping controller is guaranteed with the integration of SOA and LQR.

Section 2 deals with system background, the proposed architecture is discussed in Section 3, the methodology (SOA ad LQR) in Section 4, problem formulation and simulation diagrams in Section 5, and the results are discussed in Section 6. Sections 7 and 8 deal with the conclusion and future work.

2   System background

The traditional HP model developed for the stability analysis of a SMIBS under small perturbation is based on SG model 1.0. In this SG model 1.0 the damper winding dynamics, higher-order harmonics, and frequency deviousness are neglected. This model is simplistic with only six K-Constants representing the system dynamics. The excitation system is IEEE type-ST1. The HP model based on SG model 1.0 is called the Old Heffron-Phillips Model (OHPM). The SMIBS is shown in Figure 1. Figure 2 shows the OHPM. The SG model 1.0 involves the following equations:

$$T'_{do} \frac{dE'_q}{dt} = E'_q - (X_d - X'_d) I_d + E_{fd} \tag{1}$$

$$\frac{d\delta}{dt} = \omega - \omega_s \tag{2}$$

$$\frac{2H}{\omega_s} \frac{d\omega}{dt} = T_M - E'_q I_q - (X_q - X'_d) I_d I_q - T_{FW} \tag{3}$$

Figure 1   The SMIBS (see online version for colours)
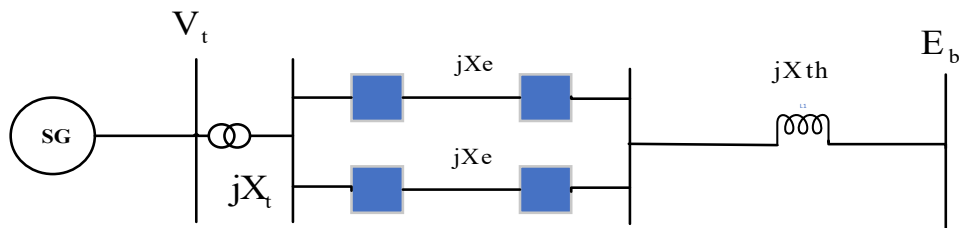

This OHPM is based on the following six K-Constants

$$K_1 = \frac{\partial P_E}{\partial \delta}, \ K_2 = \frac{\partial P_E}{\partial E'_q}, \ K_3 = \frac{\partial E_q}{\partial E'_q}, \ K_4 = \frac{\partial E_q}{\partial \delta}, \ K_5 = \frac{\partial V_t}{\partial \delta}, \ K_6 = \frac{\partial V_t}{\partial E'_q} \biggr\} \tag{4}$$

State space representation/modelling of OHPM.

$$
\begin{bmatrix} \Delta\dot{\delta} \\ \Delta\dot{\omega} \\ \Delta\dot{E}_q' \\ \Delta\dot{E}_{fd} \end{bmatrix} = \begin{bmatrix} 0 & \omega_B & 0 & 0 \\ -\dfrac{K_1}{2H} & -\dfrac{D}{2H} & -\dfrac{K_2}{2H} & 0 \\ -\dfrac{K_4}{T_{do}'} & 0 & -\dfrac{1}{T_{do}'K_3} & \dfrac{1}{T_{do}'} \\ -\dfrac{K_A K_5}{T_A} & 0 & -\dfrac{K_A K_6}{T_A} & -\dfrac{1}{T_A} \end{bmatrix} \begin{bmatrix} \Delta\delta \\ \Delta\omega \\ \Delta E_q' \\ \Delta E_{fd} \end{bmatrix} + \begin{bmatrix} 0 \\ 0 \\ 0 \\ \dfrac{K_A}{T_A} \end{bmatrix} U
$$

where U is the input control signal.

Figure 2   The Old Heffron-Phillips model (see online version for colours)
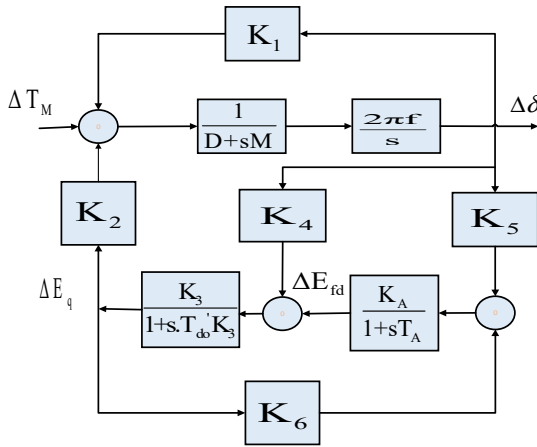
3   Proposed architecture

In this section, the mathematical modelling of the suggested AHPM which is based on SG model 1.1 is investigated. The OHPM is based on certain assumptions neglecting the dynamics of damper winding (E_d') by setting $T_{q0}' = 0$. The SG model 1.1 is a realistic model. In this SG model, 1.1 the dynamics of the internal voltage of the rotor (d-axis) and internal voltage of the rotor (q-axis) are taken into consideration. The mathematical modelling complexity is increased in this model. With the detailed modelling of SG, the stability mechanism is accurately depicted. The mathematical description of SG model 1.1 is governed by the following equations:

3.1   Equations involving the SG model 1.1

$$
T_{do}' \frac{dE_q'}{dt} = E_q' - \left(X_d - X_d' \right) I_d + E_{fd} \tag{5}
$$

$$T'_{qo} \frac{dE'_d}{dt} = -E'_d + \left(X_q - X'_q\right)I_q \tag{6}$$

$$\frac{d\delta}{dt} = \omega - \omega_s \tag{7}$$

$$\frac{2H}{\omega_s} \frac{d\omega}{dt} = T_M - E'_q I_q - E'_d I_d - \left(X'_q - X'_d\right)I_d I_q - T_{FW} \tag{8}$$

3.2 Mathematical modelling of system with SG model 1.1

This section deals with the equations of rotor angle, rotor speed, electric torque, and internal voltages with the inclusion of SG model 1.1 The IEEE type-ST1 excitation system is considered here.

$$\dot{\delta} = \omega_B \left(\omega_m - \omega_{m0}\right) \tag{9}$$

$$\dot{\omega}_m = \frac{1}{2H} \left(-k_d \left(\omega_m - \omega_{m0}\right) + T_M - T_E\right) \tag{10}$$

$$T_E = E'_d i_d + E'_q i_q + \left(x'_d - x'_q\right)i_d i_q \tag{11}$$

$$E'_q = \frac{1}{T'_{d0}} \left[\left(-E'_q + (x_d - x'_d)i_d\right) + E_{fd}\right] \tag{12}$$

$$E'_d = \frac{1}{T'_{q0}} \left[\left(-E'_d - (x_q - x'_q)i_q\right)\right] \tag{13}$$

3.3 System equations including ten K-constants

This section deals with the equations for rotor angle, speed, internal voltages, and field voltage with the inclusion of ten K-Constants. The dynamical model is linearised about its initial conditions. The linearised forms of the equations are:

$$\Delta\dot{\delta} = \omega_B \Delta\omega_m \tag{14}$$

$$\Delta\dot{\omega}_m = \frac{-D}{2H}\Delta\omega_m + \frac{1}{2H}\Delta T_M - \frac{K_1}{2H}\Delta\delta - \frac{K_2}{2H}\Delta E'_q - \frac{K_3}{2H}\Delta E'_d \tag{15}$$

$$\Delta E'_q = \frac{1}{T'_{d0}} \left(\Delta E_{fd} - K_5\Delta\delta - \frac{\Delta E'_q}{K_4}\right) \tag{16}$$

$$\Delta E'_d = \frac{1}{T'_{q0}} \left(K_7\Delta\delta - \frac{\Delta E'_d}{K_6}\right) \tag{17}$$

$$\Delta E'_{fd} = -\frac{K_A K_8}{T_A}\Delta\delta - \frac{K_A K_9}{T_A}\Delta E'_q - \frac{K_A K_{10}}{T_A}\Delta E'_d + \frac{K_A}{T_A}\Delta V_{ref} - \frac{1}{T_A}\Delta E_{fd} \tag{18}$$

3.4 K-Constants with AHPM

The SMIBS is described using various differential equations. It is assumed that the system is stable till time $t = 0$. The disturbance occurs at time $t = 0$ or later. The initial conditions (x_0) are calculated at time $t = 0$ which is based on the system's operating point. The expression and physical nature of novel K-Constants are defined as:

$$\left. \begin{array}{l} K_1 = \dfrac{\partial T_E}{\partial \delta}, \; K_2 = \dfrac{\partial T_E}{\partial E'_q}, \; K_3 = \dfrac{\partial T_E}{\partial E'_d}, \; K_4 = \dfrac{\partial E'_q}{\partial E_q}, \; K_5 = \dfrac{\partial E'_q}{\partial \delta} \\[4mm] K_6 = \dfrac{\partial E'_d}{\partial E_d}, \; K_7 = \dfrac{\partial E'_d}{\partial \delta}, \; K_8 = \dfrac{\partial E_{fd}}{\partial \delta}, \; K_9 = \dfrac{\partial E_{fd}}{\partial E'_q}, \; K_{10} = \dfrac{\partial E_{fd}}{\partial E'_d} \end{array} \right\} \quad (19)$$

The detailed expansion of these ten K-constants (novel contribution) is given in Table 1.

Table 1   K-Constants for AHPM

$$K_1 = -\left[E'_{do} + \left((x'_d - x'_q) i_{q0} \right) \right] \frac{E_{d0} E_b \sin \delta_0}{x_e + x'_d} + \left[(x'_d - x'_q) i_{d0} + E'_{qo} \right] \frac{E_b \cos \delta_0}{x_e + x'}$$

$$K_2 = -\left[E'_{d0} + \left((x'_d - x'_q) i_{q0} \right) \right] \frac{1}{x_e + x'_d} + E'_{d0} \frac{1}{x_e + x'_q} + i_{q0}$$

$$K_3 = \left[i_{d0} + \left((x'_d - x'_q) i_{d0} \right) \right] \frac{1}{x_e + x'_q} \qquad K_4 = \frac{x_e + x'_d}{(x_e + x'_d) + (x_d - x'_d)}$$

$$K_5 = (x_d + x'_d) \frac{E_b \sin \delta_0}{x_e + x'_d} \qquad K_6 = \frac{x_e + x'_q}{(x_e + x'_q) + (x_q - x'_q)}$$

$$K_7 = -(x_q + x'_q) \frac{E_b \cos \delta_0}{x_e + x'_q} \qquad K_8 = \frac{V_{do}}{V_{to}} - \left(E_b \cos \delta_0 + \frac{x_e E_b \cos \delta_0}{x_e + x'_d} \right)$$

$$K_9 = \frac{V_{qo} x_e}{V_{to}} - \frac{1}{x_e + x'_d} \qquad K_{10} = \frac{V_{do} x_e}{V_{to}} - \frac{1}{x_e + x'_q}$$

3.5 The AHPM

Figure 3 shows the AHPM based on 10 K-Constants. The AHPM model consists of the representation of flux decay, excitation system, and swing equation. The K-Constants are dependent on machine parameters and operating conditions. The various machine parameters are defined in Appendix B.

3.6 The SMIBS with PSS

The SMIBS is equipped with PSS. Figure 4 shows the PSS conventional lead-lag structure (PSS CLLS). The PSS is added to provide the additional required for stability. For this, it is required to produce an electric torque component which is in phase with the deviation in the speed $(\Delta \omega)$ of the rotor. The PSS comprises a washout block (WOB), the gain block, the phase lead-lag compensator block (PLLCB), and the limiter. The role of WOB is to eliminate/remove the steady-state bias in the PSS output. The PSS gain is selected according to the damping requirement. The PSS output is limited by the limiter.

The role of PLLCB is to provide appropriate phase compensation between input and output signals (Gandhi and Joshi, 2011).

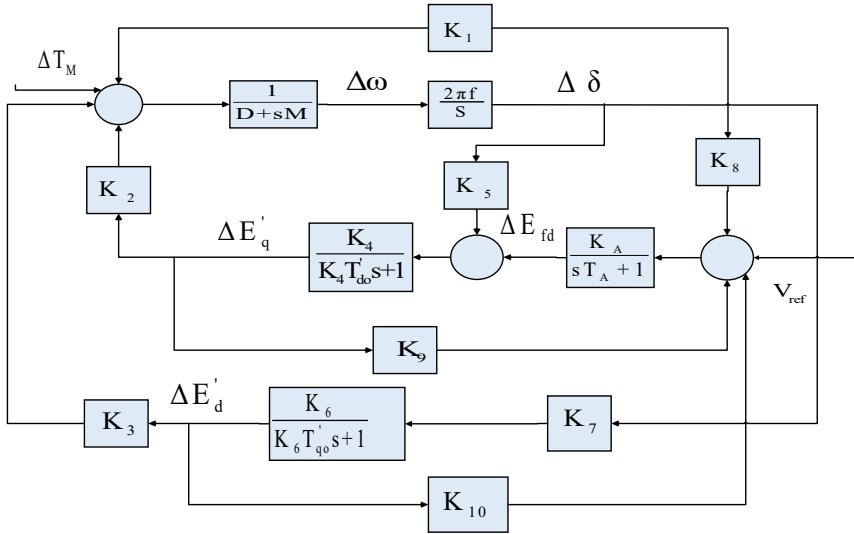**Figure 3** The AHPM (see online version for colours)
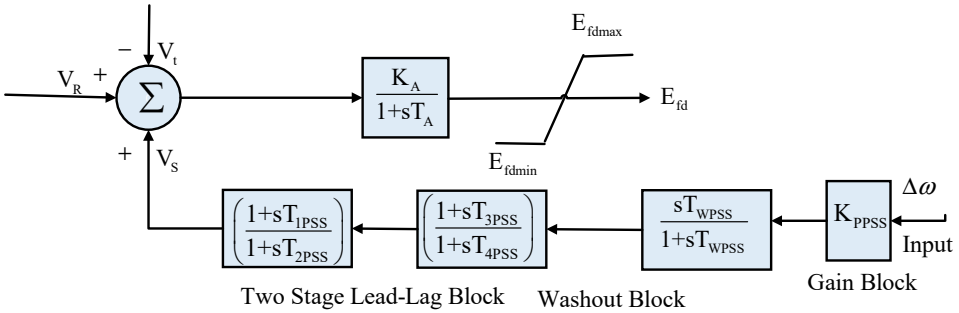

Figure 4 The PSS CLLS (see online version for colours)

The equation for the field excitation is:

$$\dot{E}_{fd} = \frac{\left(K_A \left(V_{ref} - V_t + U_{PSS}\right) - E_{fd}\right)}{T_A} \tag{20}$$

The state space representation of the SMIBS with PSS and Exciter with model 1.1

$$\begin{bmatrix} \Delta\dot{\delta} \\ \Delta\dot{\omega}_m \\ \Delta\dot{E}'_q \\ \Delta\dot{E}'_d \\ \Delta\dot{E}'_{fd} \end{bmatrix} = \begin{bmatrix} 0 & \omega_B & 0 & 0 & 0 \\ -\dfrac{K_1}{2H} & -\dfrac{D}{2H} & -\dfrac{K_2}{2H} & -\dfrac{K_3}{2H} & 0 \\ -\dfrac{K_5}{T'_{d0}} & 0 & -\dfrac{1}{T'_{d0}K_4} & 0 & -\dfrac{1}{T'_{d0}} \\ \dfrac{K_7}{T'_{q0}} & 0 & 0 & -\dfrac{1}{T'_{q0}K_6} & 0 \\ -\dfrac{K_A K_8}{T_A} & 0 & -\dfrac{K_A K_9}{T_A} & -\dfrac{K_A K_{10}}{T_A} & -\dfrac{1}{T_A} \end{bmatrix} \begin{bmatrix} \Delta\delta \\ \Delta\omega_m \\ \Delta E'_q \\ \Delta E'_d \\ \Delta E'_{fd} \end{bmatrix}$$

$$+ \begin{bmatrix} 0 \\ \dfrac{1}{2H} \\ 0 \\ 0 \\ \dfrac{K_A}{T_A} \end{bmatrix} \begin{bmatrix} 0 & \Delta T_M & 0 & 0 & V_{ref} \end{bmatrix}$$

3.7   The SMIBS with TCSC lead lag structure

The system reactance changes as a result of the TCSC being incorporated into the system. and now the total line reactance is $X_{Total} - X_e - X_{TCSC(\alpha)}$. The values of ten K-Constants also change with TCSC. The TCSC is effective for improving the system damping and power flow capacity of the system. The TCSC system consists of a capacitor in parallel with a thyristor controlled reactor (TCR). It provides variable compensation by changing the firing angle (α) of thyristors. The equation for the relation between TCSC reactance ($X_{TCSC(\alpha)}$) and firing angle (α) of TCSC (Gandi and Joshi,2014):

$$X_{TCSC(\alpha)} = X_C - \frac{X_C^2}{(X_C - X_P)} \frac{\sigma + \sin\sigma}{\pi} + \frac{4X_C^2}{(X_C - X_P)} \frac{\cos^2(\sigma/2)}{(k^2 - 1)} \frac{[k\tan(k\sigma/2) - \tan(\sigma/2)]}{\pi} \quad (21)$$

The equation showing the relation between electrical output power (P_E) of generator, rotor angle (δ) is

$$P_E = \frac{E'_q V_B}{X'_{d\Sigma}} \sin\delta + \frac{V_B^2 (X_q - X'_d)}{2X'_{d\Sigma} X'_{q\Sigma}} \sin 2\delta \quad (22)$$

Thus, by changing the firing angle, the reactance of TCSC can be adjusted, and hence the electrical output power of SG which in turn improves the damping capacity of the system. There is a change in line reactance with the inclusion of TCSC. Operating the TCSC in vernier capacitive mode the net reactance decreases and the power transfer to the system increases according to the formula:

$$P = \frac{V_S V_R}{X_L} \sin\delta \quad (23)$$

where V_S, V_R are the voltages at the sending and receiving end of the line, the (X_L) is the inductive impedance of the line and (δ) is the phase angle between the two voltages. The TCSC device is efficient in damping oscillations as well as improving the power transfer capacity of the system. Figure 5 shows the TCSC structure. The different blocks are a Gain block, a signal WOB-works as a high-pass filter, and a two-stage PLLCB having time constants T_1 to T_4. Because of the incorporation of TCSC four new constants are required in AHPM instead of three constants in the OHPM. The input is ($\Delta\omega$) and the output is the TCSC stabilising signal (Gandhi and Joshi, 2014a).

**Figure 5** The TCSC lead lag structure (see online version for colours)
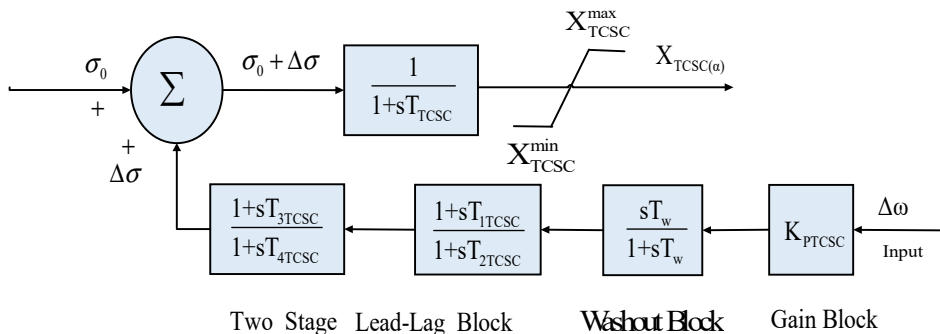
3.8 The SMIBS with PSS and TCSC (CPT)

Figure 6 shows the block diagram representation of SMIBS with PSS and TCSC. This coordinated PSS and TCSC model is called the CPT model. Proper coordination between the two devices is essential for better damping performance (Gandhi and Joshi, 2014b). The three constants due to the incorporation of TCSC based on OHPM are:

$$K_P = \frac{\partial P_E}{\partial X_{TCSC}}, K_q = \frac{\partial E_q}{\partial X_{TCSC}}, K_V = \frac{\partial V_t}{\partial X_{TCSC}} \Bigg\} \tag{24}$$

Figure 6 The SMIBS with PSS and TCSC (see online version for colours)
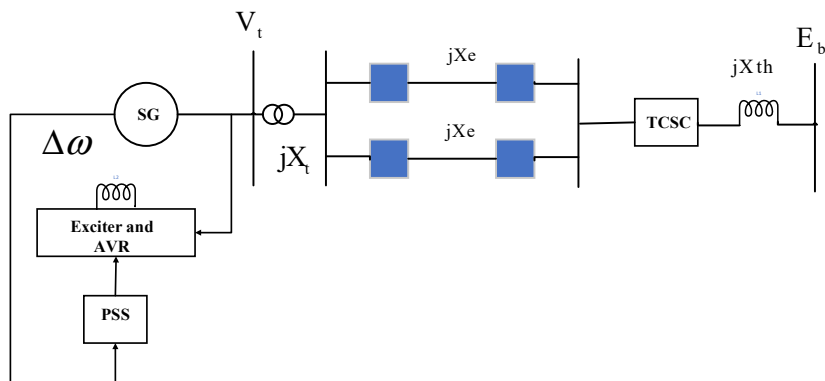
The addition of TCSC has resulted in the creation of these four new constants:

$$K_p = \frac{\partial T_E}{\partial X_{TCSC}}, K_q = \frac{\partial E'_q}{\partial X_{TCSC}}, K_d = \frac{\partial E'_d}{\partial X_{TCSC}}, K_{EFD} = \frac{\partial E_{fd}}{\partial X_{TCSC}} \Big\} \tag{25}$$

State space modelling/representation with CPT with AHPM.

$$
\begin{bmatrix} \Delta\dot\delta \\ \Delta\dot\omega_m \\ \Delta\dot E'_q \\ \Delta\dot E'_d \\ \Delta\dot E'_{fd} \end{bmatrix} =
\begin{bmatrix}
0 & \omega_B & 0 & 0 & 0 \\
-\dfrac{K_1}{2H} & -\dfrac{D}{2H} & -\dfrac{K_2}{2H} & -\dfrac{K_3}{2H} & 0 \\
-\dfrac{K_5}{T'_{d0}} & 0 & -\dfrac{1}{T'_{d0}K_4} & 0 & -\dfrac{1}{T'_{d0}} \\
\dfrac{K_7}{T'_{q0}} & 0 & 0 & -\dfrac{1}{T'_{q0}K_6} & 0 \\
-\dfrac{K_AK_8}{T_A} & 0 & -\dfrac{K_AK_9}{T_A} & -\dfrac{K_AK_{10}}{T_A} & -\dfrac{1}{T_A}
\end{bmatrix}
\begin{bmatrix} \Delta\delta \\ \Delta\omega_m \\ \Delta E'_q \\ \Delta E'_d \\ \Delta E'_{fd} \end{bmatrix}
$$

$$
+ \begin{bmatrix}
0 & 0 \\
0 & K_p \\
0 & K_q \\
0 & K_d \\
\dfrac{K_A}{T_A} & K_{Efd}
\end{bmatrix}
\begin{bmatrix} \Delta U_{PSS} \\ \Delta X_{TCSC} \end{bmatrix}
$$

Here, the state vector X is $[\Delta\delta \, \Delta\omega \, \Delta E'_q \, \Delta E'_d \, \Delta E'_{fd}]^T$ and U is the vector of input variables $[\Delta U_{PSS}, \Delta X_{TCSC}]$ (Makwana and Gandhi, 2018). The dimension of state matrix is now 5 by 5 instead of the earlier 4 by 4. The state space representation by OHPM with TCSC was:

$$
\begin{bmatrix} \Delta\dot\delta \\ \Delta\dot\omega \\ \Delta\dot E'_q \\ \Delta\dot E_{fd} \end{bmatrix} =
\begin{bmatrix}
0 & \omega_B & 0 & 0 \\
-\dfrac{K_1}{2H} & -\dfrac{D}{2H} & -\dfrac{K_2}{2H} & 0 \\
-\dfrac{K_4}{T'_{do}} & 0 & -\dfrac{1}{T'_{do}K_3} & \dfrac{1}{T'_{do}} \\
-\dfrac{K_AK_5}{T_A} & 0 & -\dfrac{K_AK_6}{T_A} & -\dfrac{1}{T_A}
\end{bmatrix}
\begin{bmatrix} \Delta\delta \\ \Delta\omega \\ \Delta E'_q \\ \Delta E_{fd} \end{bmatrix}
+ \begin{bmatrix}
0 & 0 \\
0 & \dfrac{K_p}{2H} \\
0 & \dfrac{K_q}{T'_{d0}} \\
\dfrac{K_A}{T_A} & \dfrac{K_AK_V}{T_A}
\end{bmatrix}
\begin{bmatrix} \Delta U_{PSS} \\ \Delta X_{TCSC} \end{bmatrix}
$$

4   Methodology (SOA and OCT-LQR)

In this section the proposed methodology which in the implementation of SOA and LQR is discussed.

Table 2   Different statistical parameters

S. no.	Function	Algorithm	Average	Min	Max	Median	Standard deviation
1	Unimodal	L-SHADE	1.14E+10	7.22+E09	1.88+E10	1.04+E10	3.58+E09
	F1	MFO	1.03E+10	1.20+E09	3.23+E10	5.27+E09	9.69+E09
	Shifted and rotated bent cigar function	HHO	3.97E+08	1.87+E08	1.17+E09	3.88+E08	2.46+E08
		TEO	6.23E+10	5.59+E10	7.27+E10	6.33+E10	6.16+E09
		GOA	8.23E+07	3.74+E07	2.63+E08	6.11+E07	6.07+E07
		WOA	5.32E+09	4.20+E09	9.95+E09	5.15+E09	1.71+E09
		SOA	4.65E+07	6.84+E06	1.13+E08	3.76+E07	3.28+E07
2	Multimodal function	L-SHADE	8.18E+02	7.65E+02	8.73E+02	8.21E+02	3.19E+01
	F5	MFO	6.87E+02	6.41E+02	7.66E+02	6.78E+02	3.31E+01
	Shifted and rotated Rastrigin's function	HHO	7.68E+02	7.34E+02	8.24E+02	7.77E+02	3.39E+01
		TEO	9.36E+02	9.14E+02	1.00E+03	9.33E+02	3.33E+01
		GOA	6.75E+02	6.30E+02	7.64E+02	6.76E+02	4.42E+01
		WOA	8.57E+02	8.26E+02	9.40E+02	8.52E+02	3.45E+01
		SOA	6.42E+02	5.91E+02	7.24E+02	6.29E+02	3.94E+01
3	Hybrid Function	L-SHADE	1.89E+08	2.44E+07	6.95E+08	1.42E+08	1.67E+08
	F13	MFO	1.50E+08	2.35E+04	2.91E+09	1.21E+05	6.50E+08
	N = 3	HHO	1.09E+06	7.05E+05	1.81E+06	1.09E+06	3.69E+05
		TEO	2.02E+10	1.78E+10	2.86E+10	2.15E+10	6.18E+09
		GOA	1.22E+05	6.55E+04	2.53E+05	1.07E+05	6.37E+04
		WOA	2.00E+07	3.47E+06	1.73E+08	9.32E+06	3.75E+07
		SOA	4.17E+04	8.10E+03	1.36E+05	3.84E+04	2.79E+04
4	Composition function	L-SHADE	2.60E+03	2.55E+03	2.63E+03	2.60E+03	2.40E+01
	F21	MFO	2.49E+03	2.42E+03	2.56E+03	2.48E+03	4.49E+01
	N = 3	HHO	2.60E+03	2.55E+03	2.81E+03	2.59E+03	6.49E+01
		TEO	2.82E+03	2.76E+03	2.90E+03	2.84E+03	6.35E+01
		GOA	2.48E+03	2.45E+03	2.58E+03	2.48E+03	3.71E+01
		WOA	2.64E+03	2.57E+03	2.82E+03	2.62E+03	8.83E+01
		SOA	2.43E+03	2.39E+03	2.52E+03	2.43E+03	3.25E+01

4.1   Overview of SOA

It is a novel, nature-inspired, and recently proposed (2022) optimisation algorithm in knowledge-based systems. Snakes are amazing creatures and help in maintaining the ecological balance. The four steps on which the SOA is based are the snake's mating behaviour, the source of inspiration, the mathematical modelling, the development of the algorithm and finally checking the terminating condition. The algorithm is inspired by the

unique mating behaviour of snakes. The conditions for mating are the low temperature and the availability of food. If there is no food the snakes go for the search of food or take the existing food. In the exploration phase the algorithm searches for the solution in the entire space and in the exploitation phase the algorithm searches for the solution around the promising areas. SOA maintains a good balance between the two phases (Khurma et al., 2023).

4.2   Testing with the benchmark functions

The SOA has been checked for 30 CEC 2017 benchmark functions. The three unimodal functions are the rotated and shifted bent cigar function, the sum of various power functions, and the Zakharov functions. Seven multimodal Functions are rotated and shifted Rosenbrock's, Rastrigin's, expanded Scaffer's F6, Lunacek-Bi, and non-continuous Rastrigin's, Levy, and Schwefel's functions. There are ten hybrid functions and ten composition functions. The different statistical results like average, minimum (Min), maximum (Max) value, median, and standard deviation are contrasted with different algorithms like L-SHADE, MFO, HHO, TEO, GOA, WOA, and SOA. The outcomes demonstrated greater capability and power in terms of these parameters using SOA and are shown in Table 2.

4.3   Different plots of benchmark functions

The different plots in Table 3 are the plot for the convergence curve, the box plot, the 3-D map, and the plot for the exploration and exploitation phases. The efficiency of SOA for solving the real-world optimisation problem is tested on the CEC'17 test suite. Plots for just four distinct functions are displayed.

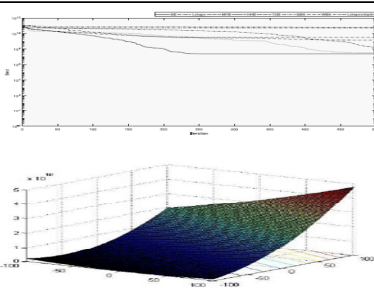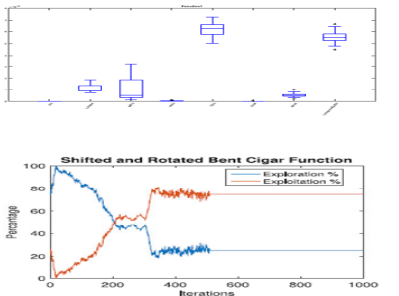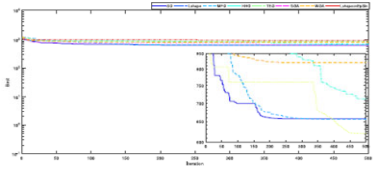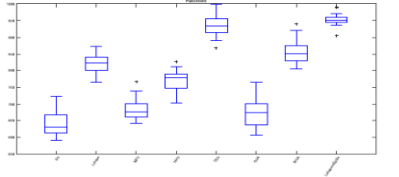**Table 3**   Plots of different functions (see online version for colours)

S. no.	Unimodal function F1

2	Multimodal function F5

Table 3   Plots of different functions (continued) (see online version for colours)

S. no.	Unimodal function F1
2	Multimodal function F5
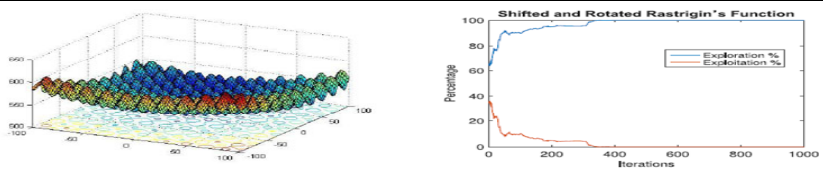
| 3 | Hybrid function F13 N = 3 |

| 4 | Composition function F21 |
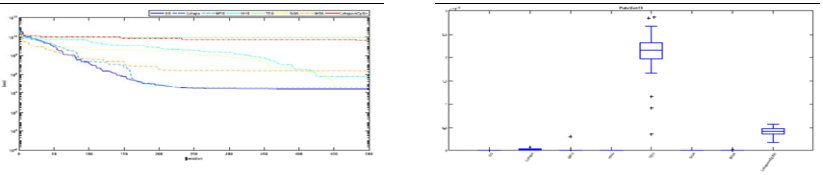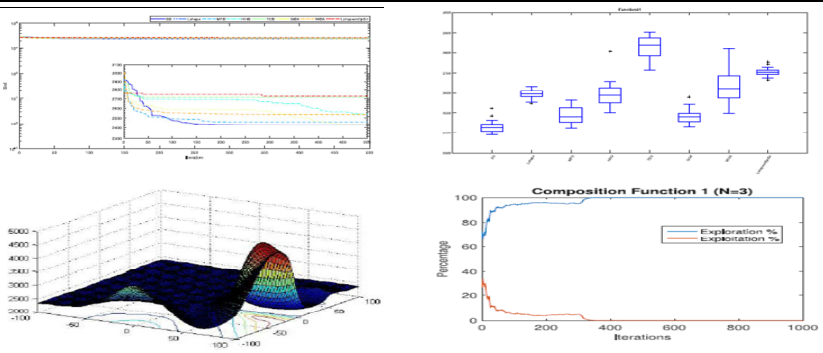
4.4   The pseudo code of SOA

Identify the problem parameters like dimensions, upper and lower bounds, population size, total or maximum_number of iterations (T), current_iteration(t)

Randomly initialisation of the population

Separating the entire population into two groups

While ($t \leq T$) do

Find N_m, N_f from both groups of male and female

Determine the best male

Determine the best female

Define the temperature using equation (S4)

Define the quantity of food using equation (S5)

If ($Q < 0.25$) then

Go for exploration phase using equations (S6) (S8)

Else if ($Q > 0.6$) then

Go for exploitation phase using equation (S10)

Else If (rand > 0.6) then

Snakes will be in mode of fighting using equation (S11) and (S12)

else

Snakes will be in mode of mating using equations (S15) and (S16)

Changing the worst female and male using equations (S19) and (S20)

end if

end if

end while

Returning the best solution

4.5   *The SOA flowchart*

Figure 7 shows the flowchart for SOA. The various equations are given and defined in Appendix C and Appendix D.

4.6   *Overview of LQR*

LQR methodology from OCT guarantees a stable and robust system that is a system not sensitive to parameter variations and external perturbations/ disturbances. The optimal solution is finding a control input (U) for minimising the quadratic cost function $J = \int_0^\infty \left(X^T Q X + U^T R U \right) dt$ (Kumara and Srinivasan, 2019). In this objective/cost function, there are two matrices Q and R which are the weighting matrices whose values can be chosen by the designer. These matrices weigh the state vector and the system input respectively. This is the benefit of LQR as there are two matrices in the cost function. The elements in Q and R regulate the excursion in state and input variables. This is defined as a regulator problem by Anderson and Moore. The system is represented in state space form ($x = Ax + Bu$) for the application of LQR. The optimal control law is defined ($U = -KX$). The optimal feedback gain matrix is ($K = R^{-1}B^TP$). The symmetric definite matrix P is the solution of the algebraic Riccati equation (ARE) ($PA + A^TP + Q - PBR^{-1}B^TP = 0$) (Gokhale et al., 2019).

For the application of LQR methodology, the system should be controllable and observable (Kumar and Jerome, 2016). The controllability and observability have been checked for the present work and the system is found to be both controllable and observable.

The state feedback gain (K) determined with LQR is passed/transferred to the CPT model which further improves the damping performance of the system. The system poles are now relocated to a more stable position with a minimum cost. The system eigenvalues

are shifted to the more left half of the s-plane indicating improvement in stability. Now the optimal eigenvalues are given by the closed loop system $\dot{x} = (A - BK)x$. Figure 8 shows the LQR methodology. Figure 9 shows the AHPM model with PSS, TCSC and LQR. The optimal feedback gain K matrix is passed to the model. This model is called CPTLQR model.

Figure 7 The SOA flowchart (see online version for colours)
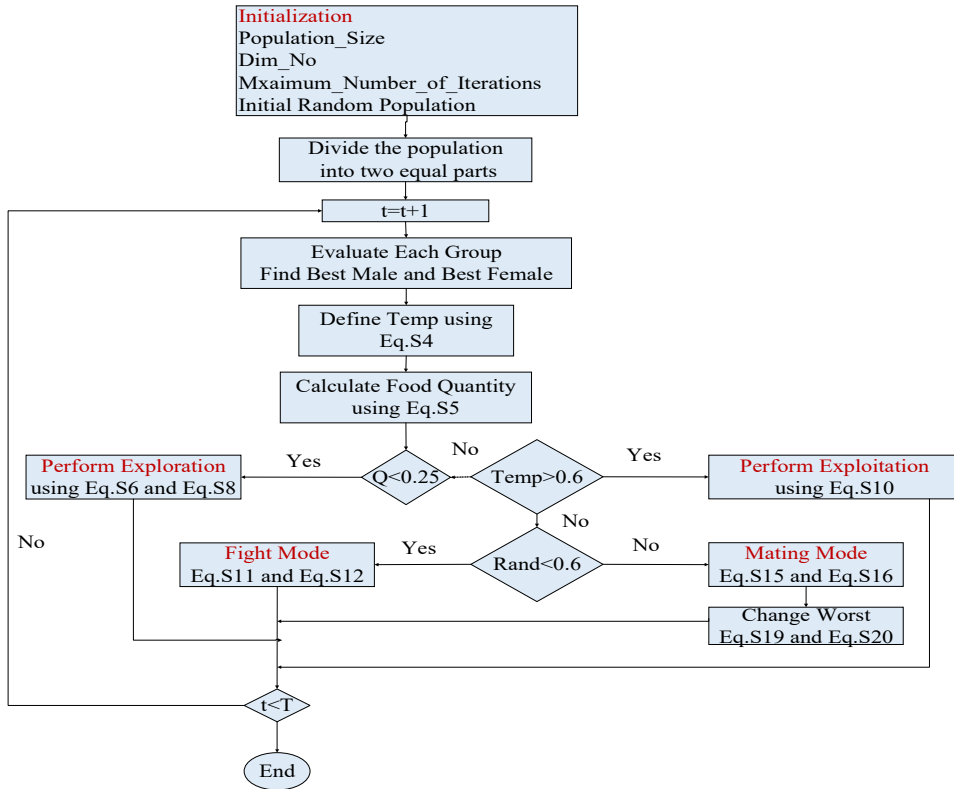
Figure 8 The LQR methodology (see online version for colours)
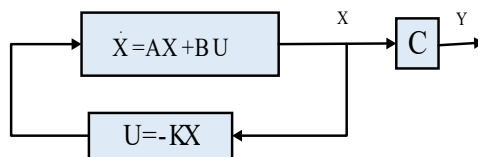
4.7 Various flowcharts

Figures 10, 11 and 12 show the flowchart with PSS, TCSC, and CPT. Figure 13 shows the LQR flowchart.

Figure 9   Coordinated PSS and TCSC with LQR (The CPTLQR) (see online version for colours)
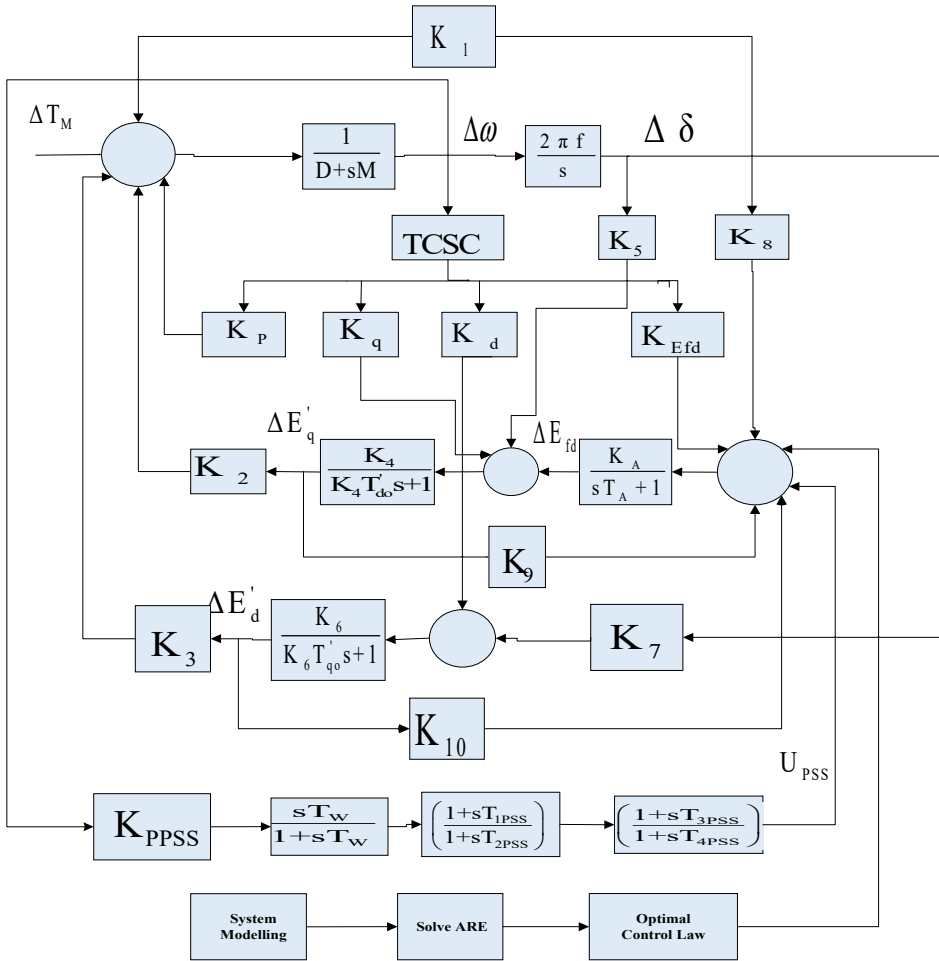
5   Problem formulation and simulation diagram

The integral time absolute error (ITAE) is selected as the objective function (OF)/ performance index. The parameters of PSS, TCSC, and CPT are obtained by SOA. The deviation in the rotor speed signal ($\Delta\omega$) has been chosen as the feedback signal for the PSS, and TCSC stabilisers. The objective is to minimise the performance index over time. The equation is $OF = \int_0^{t_{sim}} t\left|\Delta\omega(t)\right| dt$. The different constraints are given by:

$$K_{PPSS}^{MIN} \le K_{PPSS} \le K_{PPSS}^{MAX} \qquad T_{1PSS}^{MIN} \le T_{1PSS} \le T_{1PSS}^{MAX} \qquad T_{2PSS}^{MIN} \le T_{2PSS} \le T_{2PSS}^{MAX}$$

$$T_{3PSS}^{MIN} \le T_{3PSS} \le T_{3PSS}^{MAX} \qquad T_{4PSS}^{MIN} \le T_{4PSS} \le T_{4PSS}^{MAX}$$

$$K_{PTCSC}^{MIN} \le K_{PTCSC} \le K_{PTCSC}^{MAX} \qquad T_{1TCSC}^{MIN} \le T_{1TCSC} \le T_{1TCSC}^{MAX} \qquad T_{2TCSC}^{MIN} \le T_{2TCSC} \le T_{2TCSC}^{MAX}$$

$$T_{3TCSC}^{MIN} \le T_{3TCSC} \le T_{3TCSC}^{MAX} \qquad T_{4TCSC}^{MIN} \le T_{4TCSC} \le T_{4TCSC}^{MAX}$$

$$K_{BPSS}^{MIN} \le K_{BPSS} \le K_{BPSS}^{MAX} \qquad T_{1BPSS}^{MIN} \le T_{1BPSS} \le T_{1BPSS}^{MAX} \qquad T_{2BPSS}^{MIN} \le T_{2BPSS} \le T_{2BPSS}^{MAX}$$

$$T_{3BPSS}^{MIN} \le T_{3BPSS} \le T_{3BPSS}^{MAX} \qquad T_{4BPSS}^{MIN} \le T_{4BPSS} \le T_{4BPSS}^{MAX}$$

$$K_{BTCSC}^{MIN} \le K_{BTCSC} \le K_{BTCSC}^{MAX} \qquad T_{1BTCSC}^{MIN} \le T_{1BTCSC} \le T_{1BTCSC}^{MAX} \qquad T_{2BTCSC}^{MIN} \le T_{2BTCSC} \le T_{2BTCSC}^{MAX}$$

$$T_{3BTCSC}^{MIN} \le T_{3BTCSC} \le T_{3BTCSC}^{MAX} \qquad T_{4BTCSC}^{MIN} \le T_{4BTCSC} \le T_{4BTCSC}^{MAX}$$

Figure 10 Flowchart PSS model (see online version for colours)
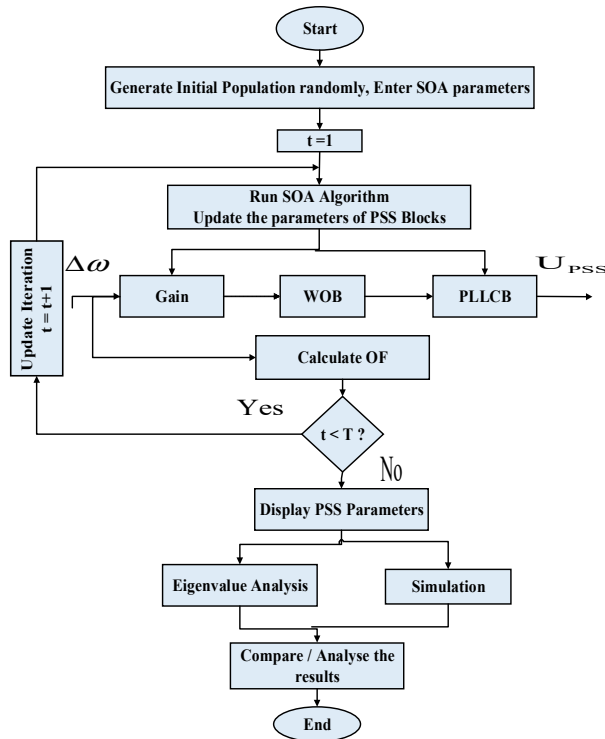
5.1 SOA parameters

The parameters of SOA are given in Table 4.

Table 4 Parameters of SOA for PSS, TCSC and CPT models

Parameter	Value
Population_Size (N)	20
Maximum_Number_of_Iterations (T)	50
Dimension (Dim)	10

Table 4   Parameters of SOA for PSS, TCSC and CPT models (continued)

Parameter	Value
No. of variables for PSS, TCSC	5.5
Upper_Bound for PSS, TCSC	1.00
Lower_Bound for PSS, TCSC	0.01
No. of variables for coordinated PSS and TCSC	10
Upper_Bound_PSS_TCSC	1.00
Lower_Bound_PSS_TCSC	0.01
Simulation time	10 seconds
T_W (washout time constant) for PSS, TCSC, CPT	10 seconds

Figure 11   Flowchart TCSC model (see online version for colours)
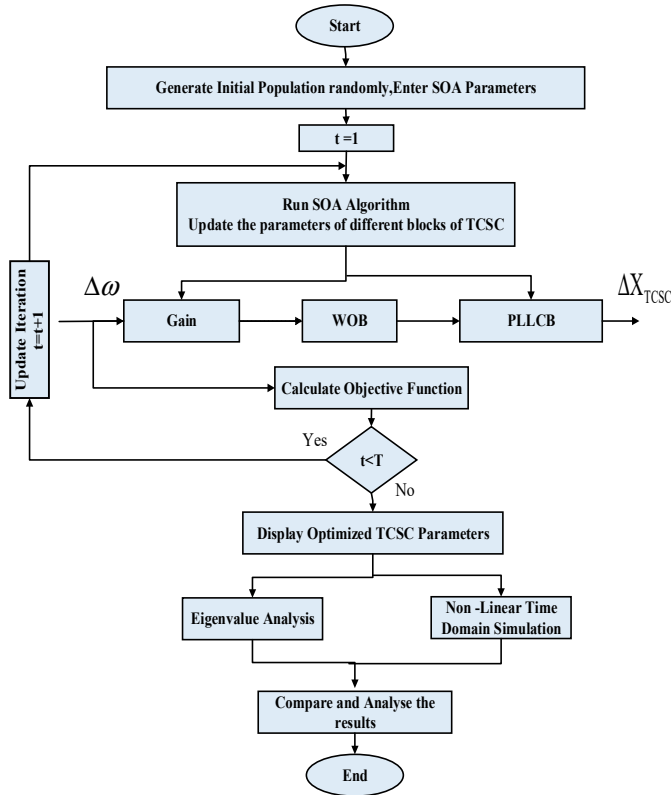
5.2   *The simulation diagram of AHPM with PSS and TCSC*

Figure 14 shows the MATLAB simulation model. The various blocks from MATLAB R 2020a are scope, display, gain constants, clock, saturation, step input, sum, and transfer function. The K-Constants are generated in the workspace and transferred to the simulation model. The simulation models are the system without any PSS or TCSC, with

PSS, with TCSC, with coordinated PSS and TCSC (CPT model), and with Coordinated PSS, TCSC, and LQR called as CPTLQR model. The gain and time constants block are inside the TCSC and PSS blocks. The system data is given in Appendix E.

Figure 12 Flowchart CPT model (see online version for colours)
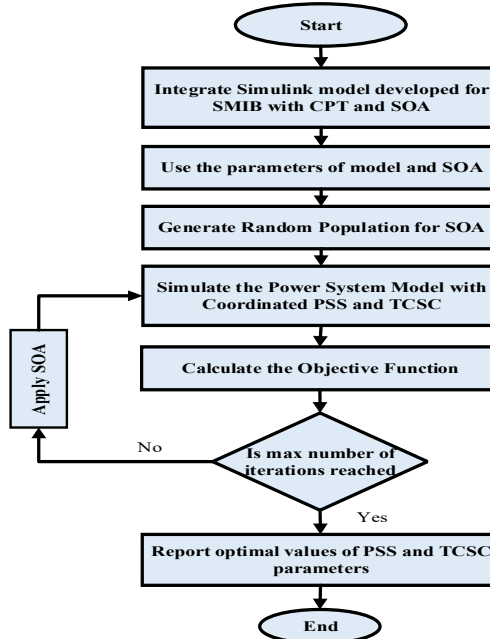
Figure 13 The LQR flowchart (see online version for colours)

Figure 14   The MATLAB simulation model with PSS and TCSC (see online version for colours)

6   Results and discussion

The time domain simulation is performed with five different simulation models for the loading condition $P = 0.6$ p.u. and $Q = 0.0224$ p.u. The parameters are tuned by simulating the different models for a 10% step increase in input mechanical power at time $t = 1.0$ second. M-files (script and function files in MATLAB) are created for the calculation of K-Constants and tuning the parameters for all the models. M-files are created for functions required in the main programming. In these functions, the gain and time constants for PSS, TCSC, and CPT models are declared. There is an M-file for SOA which is called in the M-file for tuning the parameters for the PSS, TCSC, CPT, and CPTLQR models. The K-Constants are different from the TCSC model due to the change in line reactance with TCSC. The values of these constants are passed from the workspace to the simulation models.

6.1 The K-Constants and parameters of PSS, TCSC and CPT models obtained by SOA

Table 5 and Table 6 show the values of K-Constants used in different models. The initial conditions are given in Table 7.The values of gain, time constants (in seconds), ITAE in radian/second with different models are given in Table 8.

Table 5 K-Constants for the NC and PSS models

S. no.	K-Constant	Value	S. no.	K-Constant	Value
1	K_1	0.73	6	K_6	0.76
2	K_2	1.44	7	K_7	−0.15
3	K_3	0.32	8	K_8	−0.07
4	K_4	0.45	9	K_9	0.48
5	K_5	1.07	10	K_{10}	−0.25

Table 6 K-Constants for the TCSC, CPT and CPTLQR models

S. no.	K-Constant	Value	S. no.	K-Constant	Value
1	K_1	0.80	6	K_6	0.74
2	K_2	1.53	7	K_7	−0.16
3	K_3	0.37	8	K_8	−0.08
4	K_4	0.42	9	K_9	0.46
5	K_5	1.20	10	K_{10}	−0.26

Table 7 Initial conditions

$i_{d0} = -0.383, \ i_{q0} = 0.425, \ v_{d0} = -0.674, \ v_{q0} = 0.806, \ E'_{do} = 0.232, \ E'_{qo} = 0.969, \ \delta_0 = 62°$

Table 8 Gain, time constant and ITAE obtained by SOA

PSS
$K_{PPSS} = 3.30$; $T_{1PSS} = 0.6584$; $T_{2PSS} = 0.3028$; $T_{3PSS} = 0.3855$; $T_{4PSS} = 0.7071$; ITAE = 0.0005

TCSC
$K_{PTCSC} = 3.00$; $T_{1TCSC} = 0.0100$; $T_{2TCSC} = 0.4982$; $T_{3TCSC} = 0.4002$; $T_{4TCSC} = 0.3056$; ITAE = 0.0004

Coordinated PSS and TCSC (CPT model)
$K_{BPSS} = 8.80$; $T_{1BPSS} = 0.5522$; $T_{2BPSS} = 0.3709$; $T_{3BPSS} = 0.5516$; $T_{4BPSS} = 0.9662$
$K_{BTCSC} = 0.40$; $T_{1BTCSC} = 0.2444$; $T_{2BTCSC} = 0.1269$; $T_{3BTCSC} = 0.2191$; $T_{4BTCSC} = 0.9721$; ITAE = 0.0035

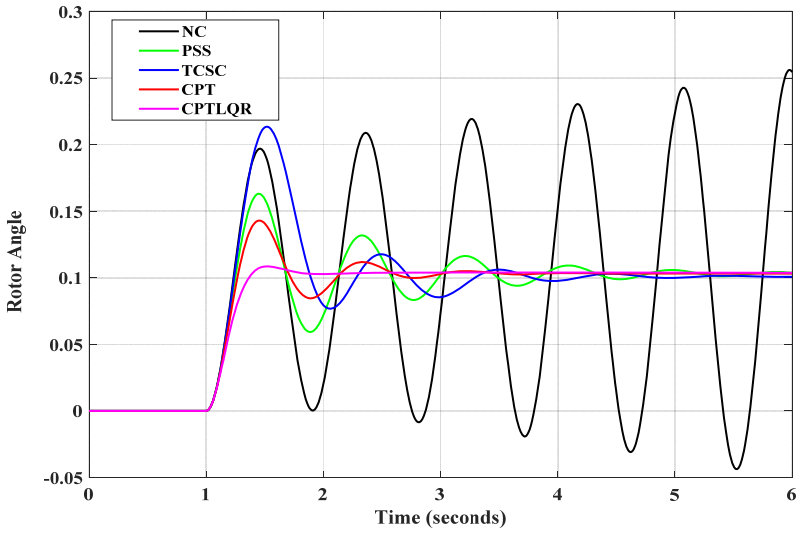| *Coordinated PSS and TCSC with LQR (CPTLQR model)* |
|---|
| $K_{BPSS} = 8.80$; $T_{1BPSS} = 0.5522$; $T_{2BPSS} = 0.3709$; $T_{3BPSS} = 0.5516$; $T_{4BPSS} = 0.9662$ |
| $K_{BTCSC} = 0.40$; $T_{1BTCSC} = 0.2444$; $T_{2BTCSC} = 0.1269$; $T_{3BTCSC} = 0.2191$; $T_{4BTCSC} = 0.9721$; ITAE = 0.0019 |

Figure 15   Rotor angle (see online version for colours)

Table 9   Rotor angle

S. no.	Undershoot	Overshoot	Settling time (seconds)
NC	–0.0438	0.2561	--
PSS	0.0000	0.1630	5.00
TCSC	0.0000	0.2134	5.10
CPT	0.0000	0.1429	3.50
CPTLQR	–0.0049	0.1085	1.50

Figure 16   Rotor speed (see online version for colours)
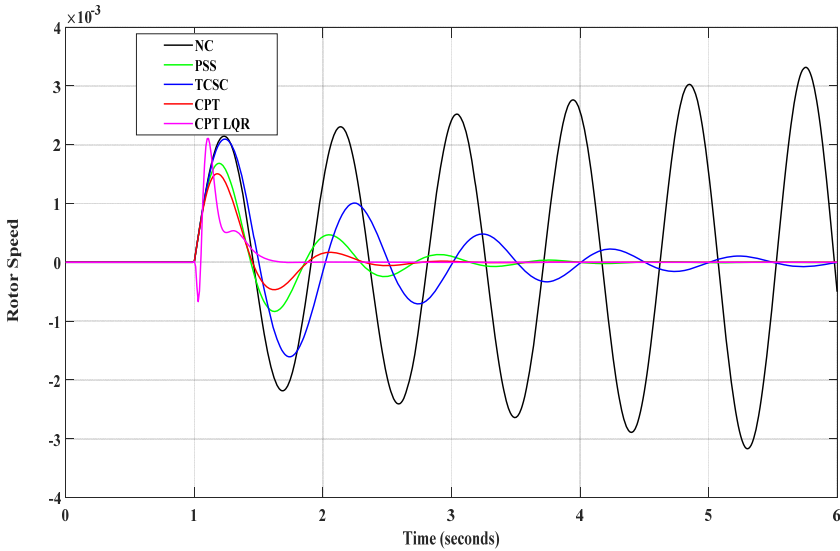
6.2 *The plot of variation of different parameters*

All of the models' responses to the step input disturbance are displayed in Figures 15 through 20. It is observed that the system with no controller (NC model is highly unstable. The system shows stability improvement in PSS, TCSC, coordinated PSS, and TCSC (CPT) models. The system is highly stable with the LQR-based Coordinated PSS and TCSC (CPTLQR) model. The oscillations and settling time (T_S) are the least with the CPTLQR model. This model is the combination of the SOA and LQR from OCT. With the appropriate values of Q and R, the feedback gain matrix *K* is obtained from the MATLAB command $K = lqr(A, B, Q, R)$. The optimal control law minimises the OF. With an LQR-based system, the poles of the system are located at the desired place leading to stability improvement. Tables 9 to 14 show the data for undershoot, overshoot, and settling time for various system parameters obtained from different models. Figure 21 shows the stabilising signal with PSS, CPT, and CPTLQR models. The oscillations are settled fastest in the CPTLQR model.

Table 10 Rotor speed

S. no.	Undershoot	Overshoot	Settling time (seconds)
NC	−0.003168	0.003315	--
PSS	−0.0008352	0.001683	4.00
TCSC	−0.001606	0.002099	6.00
CPT	−0.0004661	0.001507	2.50
CPTLQR	−0.000668	0.002107	1.80

Figure 17 Field voltage (see online version for colours)
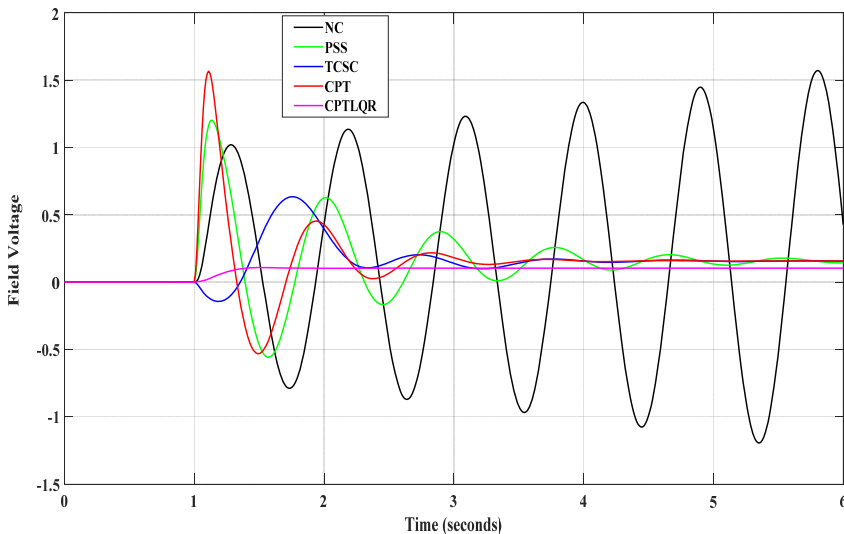
Table 11   Field voltage

S. no.	Undershoot	Overshoot	Settling time (seconds)
NC	−1.1950	1.5720	--
PSS	−0.5587	1.2020	5.00
TCSC	−0.1430	0.6347	4.00
CPT	−0.5318	1.5670	3.50
CPTLQR	0.0000	0.1085	1.50

Figure 18   The internal voltage (see online version for colours)

Figure 19   The accelerating power (see online version for colours)

Table 12 Internal voltage (q-axis)
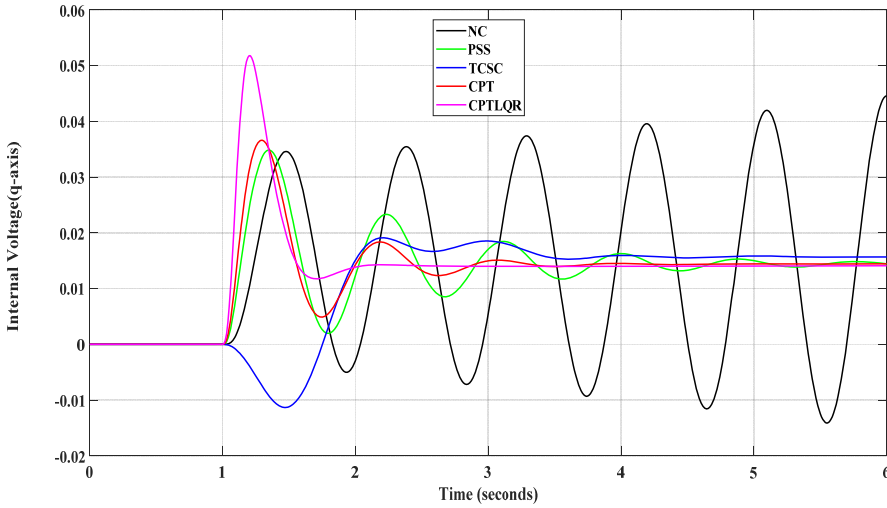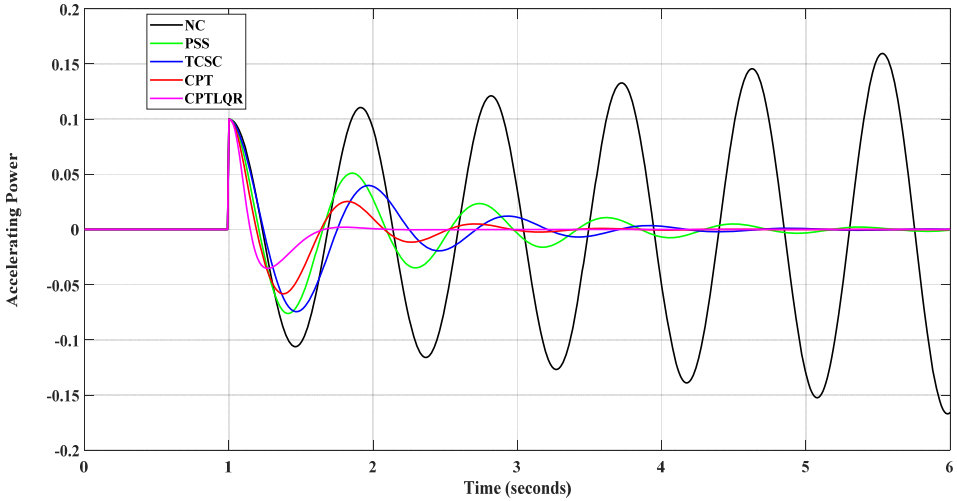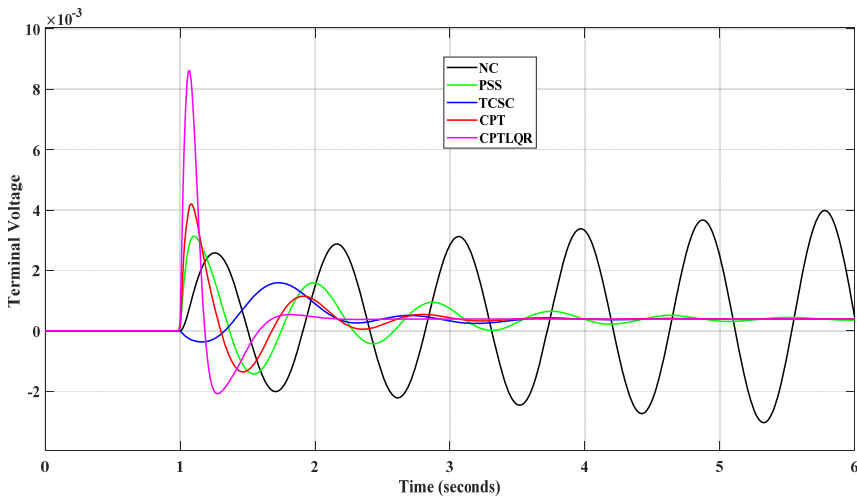
S. no.	Undershoot	Overshoot	Settling time (seconds)
NC	–0.0141	0.04459	--
PSS	0.0000	0.03485	5.00
TCSC	–0.0113	0.01909	4.00
CPT	0.0000	0.03661	3.50
CPTLQR	0.0000	0.05179	2.00

Table 13 Accelerating power

S. no.	Undershoot	Overshoot	Settling time (seconds)
NC	–0.16710	0.1596	--
PSS	–0.07614	0.1000	5.00
TCSC	–0.07447	0.09998	4.00
CPT	–0.05826	0.0995	3.50
CPTLQR	–0.03529	0.1000	1.80

Figure 20 The terminal voltage

Table 14 Terminal voltage

S. no.	Undershoot	Overshoot	Settling time (seconds)
NC	–0.003037	0.003984	--
PSS	–0.001425	0.003132	5.00
TCSC	–0.0003643	0.001596	4.00
CPT	–0.001360	0.004206	3.50
CPTLQR	–0.002079	0.008625	2.00

Figure 21   Stabilising signal (see online version for colours)
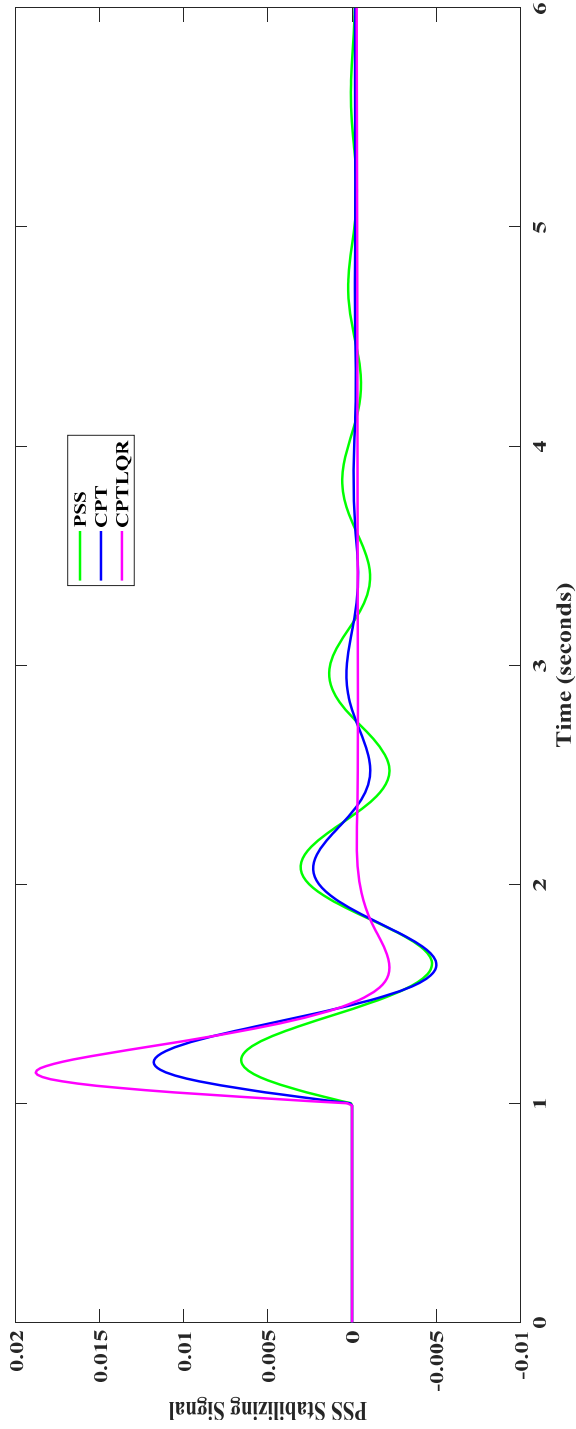
6.3 Convergence plot with PSS, TCSC and CPT

Figures 22, 23 and 24 show the convergence plot with different models. There is fast convergence with the CPT model with a lesser number of generations. The fast convergence shows the remarkable capability of SOA in optimising the problem.

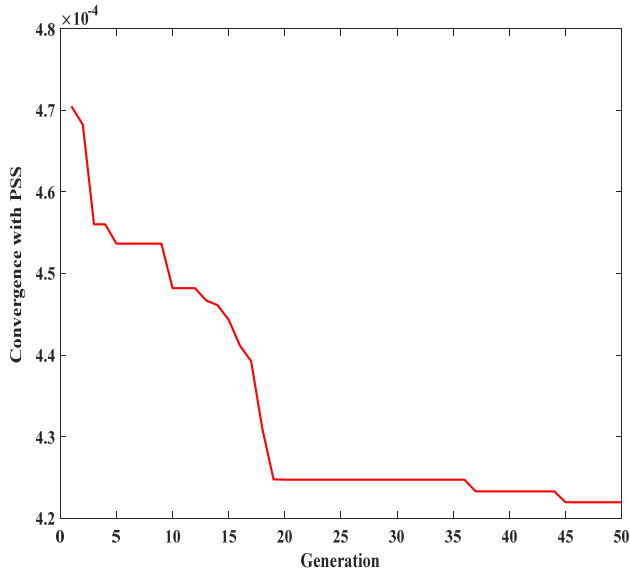**Figure 22** PSS model (see online version for colours)

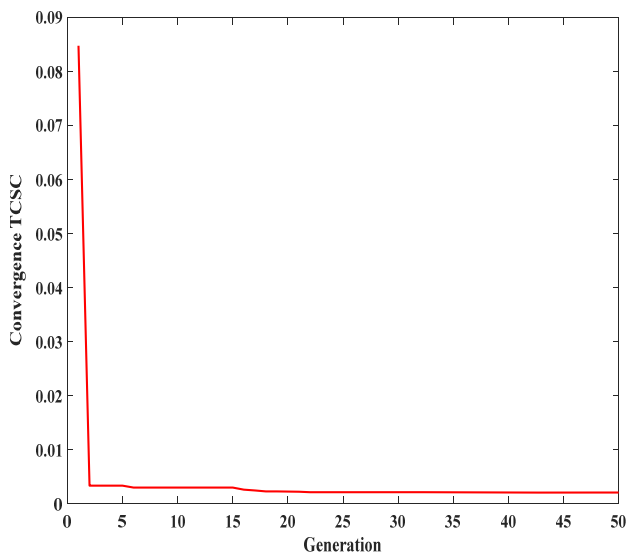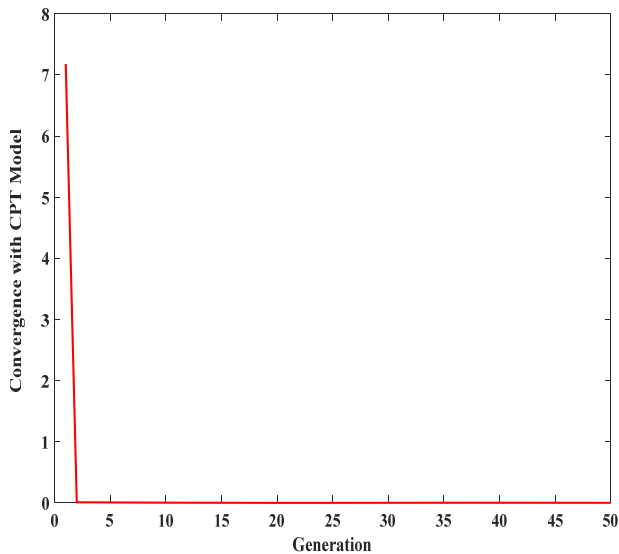**Figure 23** TCSC model (see online version for colours)

Figure 24 CPT model (see online version for colours)

6.3.1 *Contribution and novelty with SOA*

Due to proper tuning of parameters of PSS and TCSC by SOA, effective performance is obtained by different models which are justified by the variation of rotor angle, speed, voltage power, and stabilising signal. The ITAE is the least with the CPTLQR model. In SOA there is a mathematical modelling of reproduction and foraging behaviours, it is effective and efficient concerning the speed of convergence and there is a balance between exploration and exploitation. The SOA does not require a long time to converge. The convergence is fastest in the CPT model as shown in Figure 24. The SOA is a simple and efficient optimisation algorithm. There is a high performance from SOA at different operating conditions. It is used in this work because it has been tested on actual engineering problems. An analysis of the system's eigenvalues yields higher damping ratios. This is due to proper tuning by SOA. For a successful engineering design, both analysis and optimisation are essential. The analysis stage deals with the mathematical modelling and employment of scientific principles. In an optimisation process the objective function is minimised or maximised under some constraints and the optimal solution is obtained. These two components of successful engineering design are fulfilled in the present work with the use of higher order SG model 1.1 and SOA. As the order of modelling increases the complexity increases. The SOA successfully tuned the parameters of PSS and TCSC with a higher-order system's mathematical model which is justified with the results.

6.4 *Determination of system eigen values (EVS) and damping ratios (DR)*

The EVS and DR are determined for the models NC, PSS, TCSC, CPT, and CPTLQR. The system is unstable if there is one or more EVS on the right half of the complex s-plane. If all the EVS are on the left-hand side of the complex s-plane then there is a

stable system. EVS of state matrix (A) determines the system's stability. The EVS may be real or complex. The complex EVS always occurs in conjugate pairs. It is desired that all the electromechanical oscillation modes should die out as fast as possible. The EVS (λ_i) of the A matrix are calculated from the characteristic equation det $(\lambda * I - A) = 0$. By computing the EVS of the state matrix A, the system damping behaviour is analysed. The EVS ((λ_i) are given by $\lambda_i = \sigma_i \pm j\omega_i$, the DR $\xi_i = -\dfrac{\sigma_i}{\sigma_i^2 + \omega_i^2}$ and the frequency of oscillations in Hz is $f_i = -\dfrac{\omega_i}{2\pi}$. The real part of the EVS signifies the damping behaviour, and the imaginary part of the EVS shows the frequency of oscillation. The DR analysis is done for complex conjugate pairs of EVS. EVS with only the real part shows the location of poles in the s-plane.

Table 15 System EVS and DR with NC and PSS models

S. no.	(No controller) NC		PSS	
	EVS	DR	EVS	DR
1	–20.5000+25.5000i	0.6250	–12.6000+22.0000i	0.4960
2	–20.5000-25.5000i	0.6250	–12.6000-22.0000i	0.4960
3	0.1010+6.9500i	–0.0146	–7.4400+3.3400i	0.9120
4	0.1010-6.9500i	–0.0146	–7.4400-3.3400i	0.9120
5	–2.7000		–3.9400	
6			–1.0200	
7			–2.7400	
8			–1.3800	

Table 16 System EVS and DR with TCSC and CPT models

S. no.	TCSC		CPT	
	EVS	DR	EVS	DR
1	–20.2000+25.6000i	0.6180	–13.8000+22.1000i	0.5310
2	–20.2000-25.6000i	0.6180	–13.8000-22.1000i	0.5310
3	–1.6600+6.4100i	0.2500	–6.6300+5.3400i	0.7790
4	–1.6600-6.4100i	0.2500	–6.6300-5.3400i	0.7790
5	–1.3800+2.5000i	0.4820	–2.7100+0.3950i	0.9900
6	–1.3800-2.5000i	0.4820	–2.710-0.3950i	0.9900
7	–9.6600		–1.0200	
8	–2.4900		–1.0200	
9			–8.1100	
10			–0.1020	
11			–0.1000	

Table 15 shows that in the NC model there is the negative damping ratio (–0.0146) corresponding to EVS (0.1010 + 6.9500i, 0.1010-6.9500i) which shows that NC model is highly unstable. In the NC model the EVS (0.1010±6.9500i) are not lying to left half of s-plane again showing unstable system. The PSS model shows all the positive values of DR. With PSS, the damping ratios are 49.60% and 91.20% corresponding to EVS (–12.6000±22.0000i, –7.4400±3.3400i) respectively. The maximum DR with the PSS model is 91.20% which is higher than the maximum DR (62.50%) with the NC model.

Table 16 shows the system EVS and DR with TCSC and CPT models. All the DR are positive in TCSC and CPT models. In TCSC the different DRs are 61.80%, 25% and 48.20% for different EVS of system. The different DR in CPT models are 53.10%, 77.90% and 99.00%.The highest DR in TCSC model is 61.80%. The DR 99.00% is highest in CPT model. When compared to individual PSS and TCSC, the coordinated model CPT yields superior results.

Table 17   System EVS with NC and CPTLQR models

S. no.	No controller (NC)		Coordinated PSS and TCSC with LQR (CPTLQR)	
	EVS	DR	EVS	DR
1	–20.5000+25.5000i	0.6250	–100+3.4i	0.9990
2	–20.5000-25.5000i	0.6250	–100-3.4i	0.9990
3	0.1010+6.9500i	–0.0146	–150+2.5i	0.9998
4	0.1010-6.9500i	–0.0146	–150-2.5i	0.9998
5	–2.7000		–10.0000	

Table 18   Dominant EVS and DR

S. no.	Model	Dominant EVS	DR	DR(%)
1	NC	–20.5000±25.5000i	0.6250	62.50%
2	PSS	–7.4400±3.3400i	0.9120	91.20%
3	TCSC	–20.2000±25.6000i	0.6180	61.80%
4	CPT	–2.7100±0.3950i	0.9900	99.00%
5	CPTLQR	–150±2.5i	0.9998	99.98%

Figure 25   Settling time with CPTLQR (see online version for colours)
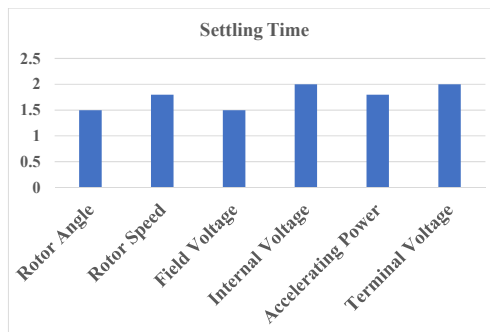
Looking at Table 17 it is found that the EVS are lying much left half of complex s-plane with LQR based controller (CPTLQR). In the CPTLQR model the DR is as high as 99.98% corresponding to EVS(–150+2.5i, –150-2.5i). The other damping ratio is also high 99.90% corresponding to EVS(–100+3.4i, –100-3.4i).The EV with only real part in NC model is –2.7000 and the EV with only real part in CPTLQR model is –10.0000. The EV with CPTLQR is lying more left of s-plane than NC model. All these results show the best model and results with CPTLQR.

Table 18 shows the dominant EVS and DR (EVS with highest DR in the respective models).

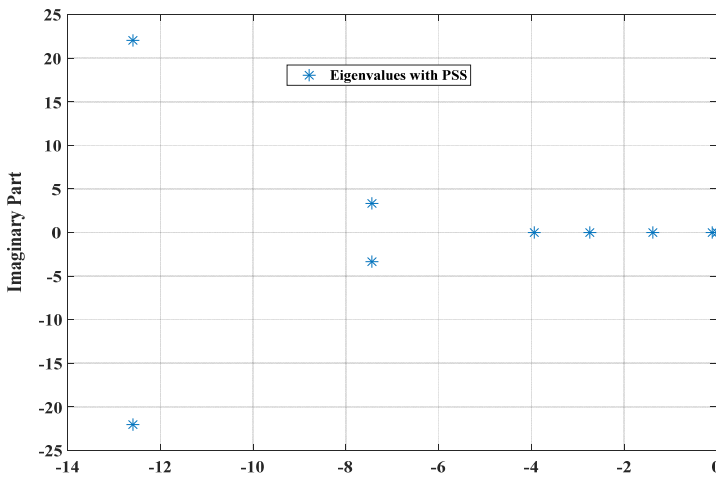**Figure 26**   EVS with PSS (see online version for colours)

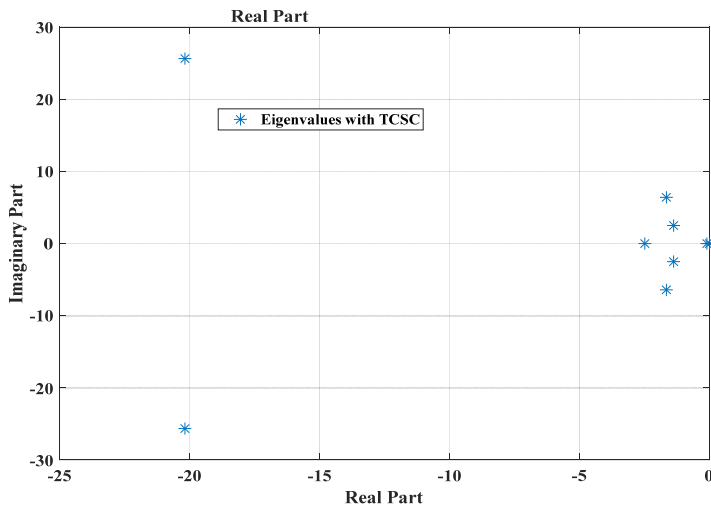**Figure 27**   EVS with TCSC (see online version for colours)

Figure 25 shows the settling time of rotor angle, rotor speed, field voltage, internal voltage, accelerating power, and terminal voltage respectively with the CPTLQR model. The settling time for these parameters is the least with this model and is between 1.5 and 2.0 seconds. The poles are placed at the desired place/location in the s-plane with the state feedback gain matrix (K) in this model. The closed-loop characteristics of the system are improved with CPTLQR and are meeting the desired damping requirement. The settling time has been contrasted with the studies of Abido (2000), Panda and Padhy (2007), Duman and Öztürk (2010), Ekinci and Hekimoglu (2017), and Alwan (2023) where the settling time is more than 2 seconds. There is a fast settling of oscillations in APHM due to better mathematical modelling as well as the combination of SOA and LQR technology. The SG model 1.1 is a more realistic model for stability studies. This agrees with the studies of Kalyani et al. (2011) which conclude that Model 1.1 is more appropriate for transient stability analysis. The SG model 2.2 though includes the effect of all the damper circuits resulting in a more unstable system. Because it does not need any kind of interface, such as high voltage transformers, storage devices, or DC links, the TCSC is an affordable and practical device (Tran et al., 2023). The power transfer capacity and voltage profile of the system have improved as a result of the addition of TCSC, which is consistent with research by Kraimia and Boudour (2021) and Arumugam and Kumar (2023). The renewables work in unforeseen conditions and increase the unpredictable conditions in the system. The power system engineers have to face grid stability and power quality issues with renewables integration into the grid (Pati, 2021; Sindhu, 2021; Xu et al., 2021). The AHPM with the inclusion of PSS, TCSC, and higher order SG model 1.1 is economical, cost-effective, and capable of meeting these challenges of renewables.

Figure 28   EVS with CPT (see online version for colours)
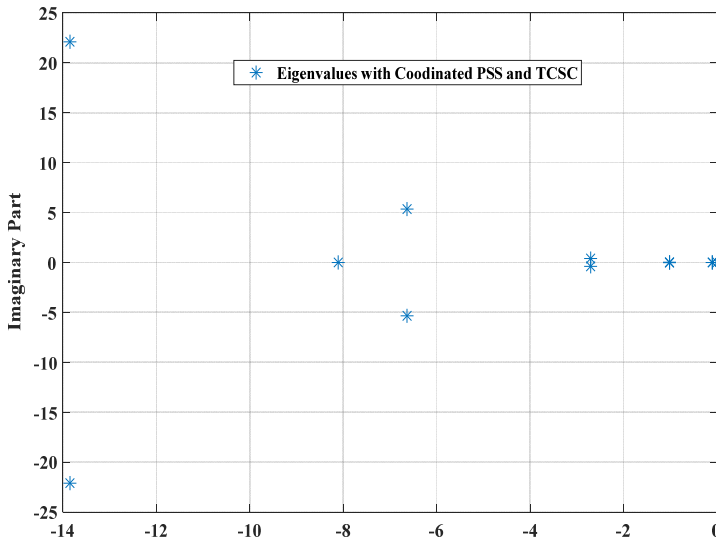
6.5 Plot of EVS with NC, PSS, TCSC and CPT models

The eigenvalues lie to the maximum left half of the s-plane with the CPTLQR model. The system whose eigenvalues lie on the left half of the s-plane has better damping characteristics. Figures 26, 27, 28 and 29 show the EVS with different models. The location of eigenvalues in the left half of the s-plane agrees with the results of Khampariya et al. (2022) and Mujeer et al. (2023).

Figure 29 EVS with CPTLQR (see online version for colours)
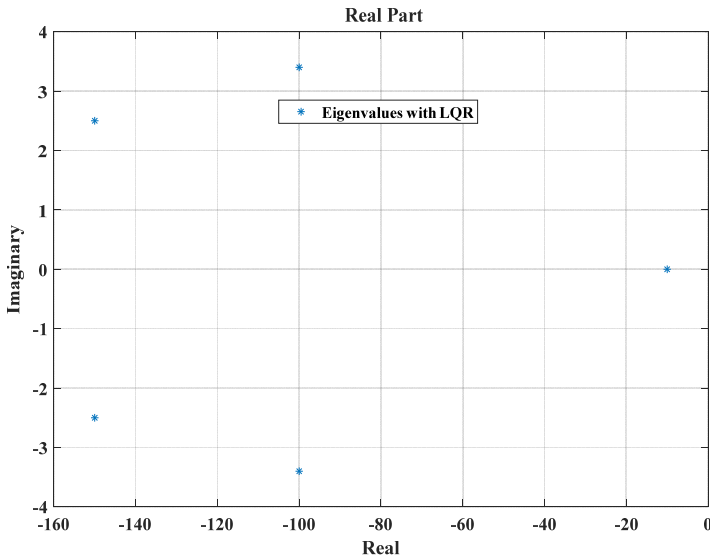
6.6 Application of feedback gain matrix K from LQR and finding eigenvalues

The system is expressed in state space form as $\dot{x} = Ax + Bu$ and $y = Cx + Du$, x, y and u represent the state, output and input vector respectively. A, B, C and D are the state, the control output and feedforward matrix respectively. The system matrices A and B without any controller are:

$$A = 1.0e+0.3* \begin{bmatrix} 0.0000 & 0.3130 & 0.0000 & 0.0000 & 0.0000 \\ -0.0001 & 0.0000 & -0.0002 & -0.0001 & 0.0000 \\ -0.0002 & 0.0000 & -0.0004 & 0.0000 & 0.0002 \\ -0.0004 & 0.0000 & 0.0000 & -0.0030 & 0.0000 \\ 1.4831 & 0.0000 & -6.9688 & 3.5782 & -0.0400 \end{bmatrix}$$

$$\text{and } B = 1.0e+0.4* \begin{bmatrix} 0.0000 \\ 0.0000 \\ 0.0000 \\ 0.0000 \\ 1.6000 \end{bmatrix}$$

The matrices

$$C = \begin{bmatrix} 1 & 0 & 0 & 0 & 0 \\ 0 & 1 & 0 & 0 & 0 \\ 0 & 0 & 1 & 0 & 0 \\ 0 & 0 & 0 & 1 & 0 \\ 0 & 0 & 0 & 0 & 1 \end{bmatrix} \quad D = \begin{bmatrix} 0 \\ 0 \\ 0 \\ 0 \\ 0 \end{bmatrix}$$

The controllability matrix

$$1.0e+10*\begin{bmatrix} 0.0000 & 0.0000 & 0.0000 & -0.0000 & 0.0007 \\ 0.0000 & 0.0000 & -0.0000 & -0.0001 & -0.0000 \\ 0.0000 & 0.0000 & -0.0000 & 0.0001 & 0.0048 \\ 0.0000 & 0.0000 & -0.0000 & 0.0001 & -0.0000 \\ 0.0000 & -0.0001 & -0.0009 & 0.0321 & -2.2601 \end{bmatrix}$$

The feedback gain K is determined using the command $K = lqr(A, B, Q, R)$. The different rules for determined the Q and R weighing matrices are:

1   The Bryson rule

$$\text{Here } Q = \begin{bmatrix} 1 & 0 & 0 & 0 & 0 \\ 0 & 1 & 0 & 0 & 0 \\ 0 & 0 & 1 & 0 & 0 \\ 0 & 0 & 0 & 1 & 0 \\ 0 & 0 & 0 & 0 & 1 \end{bmatrix} \text{ and } R = [1]$$

2   The Bouderal rule

Here $Q = C'*C$ and $R = B'*B$. In the present paper both the rules are tested for finding the K. The Q and R are also chosen by hit and trial method. The optimal feedback gain matrix K determined with the proper values of Q and R is

$$K = 1.0e+0.4*\begin{bmatrix} -0.2410 & -3.4415 & -0.0165 & 3.1727 & 0.0000 \end{bmatrix}$$

After finding K the system A matrix is modified as ALQR $= A - B*K$. The system EVS are shown in Table 19. The new A matrix is

$$ALQR = 1.0e+08*\begin{bmatrix} 0.0000 & 0.0000 & 0.0000 & -0.0000 & 0.0000 \\ 0.0000 & 0.0000 & -0.0000 & -0.0000 & -0.0000 \\ -0.0000 & 0.0000 & -0.0000 & 0.0000 & 0.0000 \\ -0.0000 & 0.0000 & 0.0000 & -0.0000 & -0.0000 \\ 0.3856 & -5.5065 & -0.0264 & -5.0763 & -0.0001 \end{bmatrix}$$

Table 19 System eigenvalues

System EVS (eig(A))	System EVS (eig(ALQR))	Conclusion
$\begin{bmatrix} -20.5000 + 25.5000i \\ -20.5000 - 25.5000i \\ 0.1010 + 6.9500i \\ 0.1010 - 6.9500i \\ -2.7010 + 0.0000i \end{bmatrix}$	$1.0e + 02 * \begin{bmatrix} -1.5000 + 0.0250i \\ -1.5000 - 0.0250i \\ -1.0000 + 0.0340i \\ -1.0000 - 0.0340i \\ -0.1000 + 0.0000i \end{bmatrix}$	These EVS are lying more left half of s-plane in LQR based system showing stability improvement.

7 Conclusions

In the present work, a robust damping controller is designed for a power system with the combination of an optimisation algorithm and LQR. An AHPM based on higher order SG model 1.1 is developed for the analysis of stability under a small perturbation with ten K-Constants governing the system dynamics.

The results are:

- The damping ratios are checked for five different models. There is negative damping in the system without any PSS or TCSC. The highest damping ratio is 0.9998 obtained with the CPTLQR model.

- The settling time for different parameters is between 1.5 to 2.0 seconds in CPTLQR. The oscillations are settled fastest with the CPTLQR model.

- The EVS are lying much left half of the s-plane in CPTLQR indicating the best damping performance. The ITAE is the least with this model.

- There is an innovative OF in LQR which comprises two functions. There is a further combination of this methodology with SOA. Hence, this work is a hybrid of two technologies, optimisation and optimal control.

- The LQR methodology guarantees a robust system with the least amount of control work, as demonstrated by the outcomes.

- There is fast convergence with SOA.

- The power transfer capacity of the present system is improved due to the inherent characteristic of TCSC without the need for investment in new stations and lines. The TCSC assures affordable and clean energy and helps in meeting the 7th goal of 17 sustainable development goals (SDGs) which are essential for the prosperity and peace of the nation.

- With the penetration of renewables in the grid, there is an introduction of intermittent characteristics in the system. The renewables bring new stability and power quality challenges for power engineers. This AHPM model due to better mathematical modelling and with the inclusion of dynamics of both internal voltages is capable of meeting these challenges.

- The stability mechanism is accurately depicted and assessed with this higher-order SG model 1.1.

- The system is now safe, secure, and reliable with this AHPM.

- A detailed and valid analysis of stability and dynamic performance is justified with this AHPM.

8   Suggestions for future work

The proposed damping controller may be designed with the help of storage technologies like superconducting magnetic energy storage (SMES) and capacitor energy storage (CES) systems. There is a rapid response with SMES and large storage with CES. A combination of SMES and CES can also be developed. But this combination involves huge costs. Hence, there is a need for affordable technology. Other storage technology like battery energy storage can be used in research work.

References

Abdulkader, R., Ghanimi, H.M., Dadheech, P., Alharbi, M., Fouda, M.M., Aly, M.H., Swaminathan, D. and Sengan, S. (2023) 'Soft computing in smart grid with decentralized generation and renewable energy storage system planning', *Energies*, Vol. 16, No. 6, pp.1–24.

Abido, M.A. (2000) 'Pole placement technique for PSS and TCSC-based stabilizer design using simulated annealing', *Electrical Power and Energy Systems*, Vol. 22, No. 8, pp.543–554 [online] https://www.sciencedirect.com/science/article/abs/pii/S0142061500000272.

Alwan, H.O. (2023) 'A novel approach for coordinated design of TCSC controller and PSS for improving dynamic stability in power systems', *Periodicals of Engineering and Natural Sciences*, Vol. 11, No. 2, pp.102–116.

Aribowo, W. (2023) 'A novel improved sea-horse optimizer for tuning parameter power system stabilizer', *Journal of Robotics and Control*, Vol. 4, No. 1, pp.12–22.

Aribowo, W., Muslim, S., Suprianto, B., Haryudo, S.I. and Joko (2021) 'Tunicate swarm algorithm-neural network for adaptive power system stabilizer parameter', *Science and Technology Asia*, Vol. 26, No. 3, pp.50–63.

Aribowo, W., Suprianto, B., Kartini, U.T. and Prapanca, A. (2023) 'Dingo optimization algorithm for designing power system stabilizer', *Indonesian Journal of Electrical Engineering and Computer Science*, Vol. 29, No. 1, pp.1–7.

Arumugam, V. and Kumar, A. (2023) 'Embedded control system for reactive power control in distributed energy resources for voltage regulation in the distributed power system', Serbian *Journal of Electrical Engineering*, Vol. 20, No. 1, pp.107–126.

Behzadpoor, S., Davoudkhani, I.F., Abdelaziz, A.Y., Geem, Z.W. and Hong, J. (2022) 'Power system stability enhancement using robust FACTS-based stabilizer designed by a hybrid optimization algorithm', *Energies*, Vol. 15, No. 22, pp.1–30.

Chaib, L., Choucha, A., Arif, S., Zaini, H.G. and Ghoneim, S.S. (2021) 'Robust design of power system stabilizers using improved harris hawk optimizer for interconnected power system', *Sustainability*, Vol. 13, No. 21, pp.1–18.

Dao, M.T., Truong, K., Do, D.N., Truong, B.H., Nguyen, K.P. and Ngoc, D. (2023) 'Security-constrained temperature-dependent optimal power flow using hybrid pseudo-gradient based particle swarm optimization and differential evolution', *International Journal on Electrical Engineering and Informatics*, Vol. 15, No. 1, pp.82–105.

Duman, S. and Öztürk, A. (2010) 'Robust design of PID controller for power system stabilization by using real coded genetic algorithm', *International Review of Electrical Engineering*, Vol. 5, No. 5, pp.2159–2170.

Ekinci, S. and Hekimoglu, B. (2017) 'Coordinated design of TCSC and PSS by using PSO algorithm for enhancement of SMIB power system stability', *Batman University Journal of Life Sciences*, Vol. 7, Nos. 1/2, pp.9–21.

Gandhi, P.R. and Joshi, S.K. (2011) 'GA based conventional and PID power system stabilizer for stability analysis of SMIB system', *Elixir International Journal on Electrical Engineering*, Vol. 40, No. 20, pp.5229–5233.

Gandhi, P.R. and Joshi, S.K. (2014a) 'Design of power system stabilizer using genetics algorithm based neural network', I*nternational Journal on Electrical Engineering*, Vol. 14, No. 2, pp.1–13.

Gandhi, P.R. and Joshi, S.K. (2014b) 'Smart control techniques for design of TCSC and PSS for stability analysis of dynamical power system', *Applied Soft Computing*, Vol. 24, No. C, pp.654–668, Elsevier.

Gokhale, S.S., Kulkarni, S.P. and Yathisha, L. (2019) 'Optimal and non-optimal based feedback switching control techniques for the turbocharged diesel engines', *International Journal of Research in Advent Technology*, Vol. 7, No. 4, pp.608–615.

Hashim, F.A. and Hussien, A.G. (2022) 'Snake optimizer: a novel meta-heuristic optimization algorithm', *Knowledge-Based Systems*, Vol. 242, pp.1–34, Elsevier [online] https://www.sciencedirect.com/science/article/abs/pii/S0950705122001150.

He, P., Jin, H., Zheng, M. and Shen, R. (2022) 'Coordinated design of PSS and multiple FACTS devices based on the improved steepest descent algorithm to improve the small-signal stability of wind-PV grid-connected system', *Journal of Electrical Systems*, Vol. 18, No. 2, pp.173–192.

Izci, D. (2022) 'A novel modified arithmetic optimization algorithm for power system stabilizer design', *Sigma Journal of Engineering and Natural Sciences*, Vol. 40, No. 3, pp.529–541.

Izdebski, M., Małkowski, R. and Miller, P. (2022) 'New performance indices for power system stabilizers', *Energies*, Vol. 15, No. 24, pp.1–23.

Jokarzadeh, M., Abedini, M. and Seifi, A. (2019) 'Improving power system damping using a combination of optimal control theory and differential evolution algorithm', *ISA Transactions*, Vol. 90, No. 2019, pp.169–177.

Kalyani, S., Prakash, M. and Ezhilarasi, G.A. (2011)' Transient stability studies in SMIB system with detailed machine models', *International Conference on Recent Advancements in Electrical, Electronics and Control Engineering*, Sivakasi, India, pp.459–464, DOI: 10.1109/ICONRAEeCE.2011.6129781.

Khampariya, P., Panda, S., Alharbi, H., Abdelaziz, A.Y. and Ghoneim, S.S. (2022) 'Coordinated design of type-2 fuzzy lead-lag-structured SSSCs and PSSs for power system stability improvement', *Sustainability*, Vol. 14, No. 11, pp.1–21.

Khurma, R.A., Albashish, D., Braik, M., Alzaqebah, A., Qasem, A. and Adwan, O. (2023) 'An augmented snake optimizer for diseases and COVID-19 diagnosis', *Biomedical Signal Processing and Control*, Vol. 84, pp.1–20, Elsevier.

Kim, J.S. and Ahn, C.W. (2021) 'Expediting population diversification in evolutionary computation with quantum algorithm', *International Journal of Bio-Inspired Computation*, Vol. 17, No. 1, pp.63–73.

Kraimia, M.N. and Boudour, M. (2021) 'Harmonic analysis of thyristor-controlled series capacitor in polluted Algerian network', International Journal of Energy Technology and Policy, Vol. 17, No. 1, pp.86–97.

Kumar, E.V. and Jerome, J. (2016) 'Algebraic Riccati equation-based Q and R matrices selection algorithm for optimal LQR applied to tracking control of 3rd order magnetic levitation system', *Archives of Electrical Engineering*, Vol. 65, No. 1, pp.151–168.

Kumara, K. and Srinivasan, A.D. (2019) 'Comparison and assessment of conventional and optimal coordinated PSS and UPFC damping controller', *International Journal of Engineering and Advanced Technology*, Vol. 8, No. 5, pp.389–393.

Latif, S., Irshad, S., Ahmadi, K.M., Shokouhandeh, H., Colak, I. and Eguchi, K. (2022) 'Intelligent design of multi-machine power system stabilizers (PSSs) using improved particle swarm optimization', *Electronics*, Vol. 11, No. 6, pp.1–15.

Makwana, A.M. and Gandhi, P.R. (2018) 'Day-ahead wind energy forecasting using feed forward neural network', *Advances in Intelligent Systems and Computing*, Vol. 671, pp.221–233, Springer, Singapore.

Mujeer, S.A., Dwarasila, M.K., Chintala, J.D. and Adimulam, V.S. (2023) 'Low frequency oscillations damping by design of power system stabilizer using intelligent controllers *Materials Today: Proceedings*, Elsevier, Vol. 80, No. 3.pp.2862–2871.

Noco, A. and Paszek, S. (2023) 'A comprehensive review of power system stabilizers', *Energies*, Vol. 16, No. 4, p.16, pp.1–32.

Panda, S. and Padhy, N.P. (2007) 'Coordinated design of TCSC controller and PSS employing particle swarm optimization technique', *International Journal of Electrical and Computer Engineering*, Vol. 1, No. 4, pp.698–706.

Panda, S., Mohanty, P.K. and Sahu, B.K. (2013) 'Bacteria foraging optimisation algorithm for tuning of PSS and STATCOM-based controller parameters', *International Journal of Data Mining, Modelling and Management*, Vol. 5, No. 4, pp.351–369.

Parvandeh, S., Boroomand, M., Boroumand, F. and Soltani, P. (2021) 'A modified single and multi-objective bacteria foraging optimisation for the solution of quadratic assignment problem', *International Journal of Bio-Inspired Computation*, Vol. 17, No. 1, pp.1–13.

Pati, S. (2021) 'India's sustainable energy future and the challenges for optimised integration of variable energy sources', *International Journal of Energy Technology and Policy*, Vol. 17, No. 1, pp.98–116.

Reddy, K.H. and Ramanathan, P. (2017) 'A new feedback gain matrix based LQR PI controller for Integrator time delay process', *Journal of Science*, Vol. 30, No. 4, pp.232–251.

Sahu, P.R., Hota, P.K., Panda, S., Lenka, R.K., Padmanaban, S.K. and Blaabjerg, F. (2022a) 'Coordinated design of FACTS controller with PSS for stability enhancement using a novel hybrid whale optimization algorithm – Nelder Mead approach', *Electric Power Components and Systems*, Vol. 49, Nos. 16–17, pp.1–28.

Sahu, P.R., Lenka, R.K., Khadanga, R.K., Hota, P.K., Panda, S. and Ustun, T.S. (2022b) 'Power system stability improvement of FACTS controller and PSS design: a time-delay approach', *Sustainability*, Vol. 14, No. 21, pp.1–23.

Samal, D., Bisoi, R. and Sahu, B. (2021) 'Identification of nonlinear dynamic system using machine learning techniques', *International Journal of Power and Energy Conversion*, Vol. 12, No. 1, pp.23–43.

Shankar, S., Veeramanju, K.T. and Yathisha, L. (2019) 'Multi-stage switching control of multi-LQR's for STATCOM operating over wide range of operating conditions in power system', *International Journal of Recent Technology and Engineering*, Vol. 7, No. 6S, pp.371–379.

Sindhu, S. (2021) 'Assessment, simulation and analysis of PV power generation for educational buildings of a rural women's university in India: a case study', *International Journal of Energy Technology and Policy*, Vol. 17, No. 1, pp.61–85.

Soliman, M., Bendary, F., Mansour, W. and Elshafei, A.L. (2011) 'LMI static output feedback design of fuzzy power system stabilisers', *International Journal of Modelling, Identification and Control*, Vol. 12, No. 4, pp.328–340.

Sun, M., Guo, Y. and Song, S. (2021) 'The delay-dependent DOFC for damping inter-area low-frequency oscillations in an interconnected power system considering packet loss of wide-area signals', *Energies*, Vol. 14, No. 18, pp.1–19.

Thu, W.M. and Lin, K.M. (2021) 'Statistical t-test assessment on performance of power system stabilizer for oscillation damping', *International Journal of Applied Power Engineering*, Vol. 10, No. 3, pp.271–280.

Tran, D.T., Ha, P.T., Nguyen, H.D. and Nguyen, T.T. (2023) 'Apply three metaheuristics algorithms for energy storage-based integrated power system to reduce generation cost', *Bulletin of Electrical Engineering and Informatics*, Vol. 12, No. 2, pp.633–641.

Xu, B., Lei, L., Zhao, Z., Jiang, W., Xiao, S., Li, H., Zhang, J. and Chen, D. (2021) 'Low frequency oscillations in a hydroelectric generating system to the variability of wind and solar power', *Water*, Vol. 13, No. 14, pp.1–23.

Appendix A

Table A1   Nomenclature

Abbreviations	Description
FACTS	Flexible alternating current transmission system
TCSC	Thyristor controlled series capacitor
SSR	Sub synchronous resonance
IEEE	Institute of Electrical and Electronics Engineers
L-SHADE	Linear population size reduction-success history adaptation for differential evolution
MFO	Moth flame optimisation
HHO	Harris hawk optimisation
TEO	Thermal exchange optimisation
GOA	Grasshopper optimisation algorithm
WOA	Whale optimisation algorithm
CEC	Congress on evolutionary computing

Appendix B

Table B1   Various machine parameters

Symbols	Description
T'_{d0}	Open circuit d-axis time constant or the transient time constant of d-axis in sec
T'_{q0}	Open circuit q-axis time constant or the transient time constant of q-axis in sec
T''_{d0}	Sub-transient time constant of d-axis in sec
T''_{q0}	Sub-transient time constant of q-axis in sec
E'_d	d-axis transient voltage in p.u
E'_q	q-axis transient voltage in p.u
E_{fd}	Field Voltage in p.u.
E_b	Infinite bus voltage in p.u.
x_d	d-axis synchronous reactance in p.u.
x_q	q-axis synchronous reactance in p.u.
x'_d	d-axis transient reactance in p.u.

Table B1   Various machine parameters (continued)

Symbols	Description
x'_q	q-axis transient reactance in p.u.
x''_d	Sub-transient reactance in d-axis in p.u.
x''_q	Sub transient reactance in q-axis in p.u.
i_d	d-axis current
i_q	q-axis current
ω	Rotor speed radian/second
ω_s	Synchronous speed radian/second
ω_B	Rotor base speed radian/second
ω_m	Generator slip in p.u.
ω_{m0}	Initial operating slip in p.u.
T_M	Mechanical torque in p.u.
T_E	Electrical torque in p.u.
T_{FW}	Additional damping torque
K_A	Gain constant of excitation system
T_A	Time constant of excitation system
V_t	Terminal voltage
V_{ref}	Reference voltage
P_M	Input mechanical power of the generator
P_E	Output electrical power of the generator
S_m	Generator slip in p.u.
S_{m0}	Initial operating slip in p.u.
M	Inertia constant
k_d or D	Damping coefficient
H	Inertia constant
x_e	line reactance
$x_{TCSC(\alpha)}$	Reactance of TCSC at firing angle (α)
x_{net}	Total system reactance
v_d	d-axis voltage
v_q	q-axis voltage
ψ_{1d}	Flux linkage on d-axis damper winding/coils
ψ_{2d}	Flux linkage on q-axis damper windings/coils
P	Active power in p.u.
Q	Reactive power in p.u.

Appendix C

Table C1   Equations with SOA

$X_i = X_{min} + rx(X_{max} - X_{min})$	S1
$N_m = N/2$	S2
$N_f = N - N_m$	S3
$\text{Temp} = Exp\left(\dfrac{-t}{T}\right)$	S4
$Q = c_1 * \exp\left(\dfrac{t-T}{T}\right)$	S5
$X_{i,m}(t+1) = X_{rand,m}(t+1) \pm c_2 \times A_m \times ((X_{max} - X_{min}) \times \text{rand} + X_{min})$	S6
$A_m = \exp\left(\dfrac{-f_{rand,m}}{f_{i,m}}\right)$	S7
$X_{i,f} = X_{rand,f}(t+1) \pm c_2 \times A_f \times ((X_{max} - X_{min}) \times \text{rand} + X_{min})$	S8
$A_f = \exp\left(\dfrac{-f_{rand,f}}{f_{i,f}}\right)$	S9
$X_{i,j}(t+1) = X_{food} \pm c_3 \times Temp \times \text{rand} \times (X_{food} - X_{i,j}(t))$	S10
$X_{i,m}(t+1) = X_{i,m}(t) + c_3 \times FM \times \text{rand} \times (Q \times X_{best,f} - X_{i,m}(t))$	S11
$X_{i,f}(t+1) = X_{i,f}(t+1) + c_3 \times FF \times \text{rand} \times (Q \times X_{best,m} - X_{i,F}(t+1))$	S12
$FM = \exp\left(\dfrac{-f_{best,f}}{f_i}\right)$	S13
$FF = \exp\left(\dfrac{-f_{best,m}}{f_i}\right)$	S14
$X_{i,m}(t+1) = X_{i,m}(t) + c_3 \times M_m \times \text{rand} \times (Q \times X_{i,f}(t) - X_{i,m}(t))$	S15
$X_{i,f}(t+1) = X_{i,f}(t) + c_3 \times M_f \times \text{rand} \times (Q \times X_{i,m}(t) - X_{i,f}(t))$	S16
$M_m = \exp\left(\dfrac{-f_{i,f}}{f_{i,m}}\right)$	S17
$M_f = \exp\left(\dfrac{-f_{i,m}}{f_{i,f}}\right)$	S18
$X_{worst,m} = X_{min} + \text{rand} \times (X_{max} - X_{min})$	S19
$X_{worst,f} = X_{min} + \text{rand} \times (X_{max} - X_{min})$	S20

Appendix D

Table D1   SOA parameters

Symbols	Description
N	Number of individuals
N_m	Number of male members
N_f	Number of female members
t	Current iteration
T	Maximum no of iterations
A_m	Male ability to find the food
A_f	Female ability to find the food
$f_{i,m}$	fitness of ith individual in male group
$f_{i,f}$	fitness of ith individual in female group
$f_{rand,f}$	Fitness of $X_{rand,f}$
$f_{rand,m}$	Fitness of $X_{rand,m}$
f_{food}	Position of Food
$f_{best,m}$	Best male
$f_{best,f}$	Best female
FF	Female fighting ability
FM	Male fighting ability
Q	Food quantity
rand	Random number between 0 and 1
X_i	i^{th} individual position
$X_{i,m}$	i^{th} male position
$X_{i,f}$	i^{th} female position
X_{max}	Problem upper bound
X_{min}	Problem lower bound
$X_{rand,f}$	Random position in female group
$X_{rand,m}$	Random position in male group
$X_{worst,f}$	Worst individual in female group
M_m	Mating ability of male
M_f	Mating ability of female
$X_{worst,m}$	Worst individual in male group
Temp	Temperature

Appendix E

Table E1   System data based on 1,000 MVA

Generator		Transmission line		Operating data	
x_d	1.76	R_t	0.086	E_b	1.00
x_q	1.58	x_l	0.813	V_t	1.05
x'_d	0.43	B_c	0.118	θ	21.66º
x'_q	1.04	Excitation system		X_{TH}	0.14
T'_{d0}	6.66	K_A	400		
T'_{q0}	0.44	T_A	0.025		
H	3.54				
ω_B	314 rad/sec				